Beyond Poisson–Boltzmann: fluctuations and fluid structure in a self-consistent theory

**Topical Review**

# Beyond Poisson–Boltzmann: fluctuations and fluid structure in a self-consistent theory

## S Buyukdagli[1] and R Blossey[2]

[1] Department of Physics, Bilkent University, Ankara 06800, Turkey
[2] University of Lille 1, CNRS, UMR 8576 UGSF—Unité de Glycobiologie Structurale et Fonctionnelle, 59000 Lille, France

E-mail: buyukdagli@fen.bilkent.edu.tr

**Abstract**

Poisson–Boltzmann (PB) theory is the classic approach to soft matter electrostatics and has been applied to numerous physical chemistry and biophysics problems. Its essential limitations are in its neglect of correlation effects and fluid structure. Recently, several theoretical insights have allowed the formulation of approaches that go beyond PB theory in a systematic way. In this topical review, we provide an update on the developments achieved in the self-consistent formulations of correlation-corrected Poisson–Boltzmann theory. We introduce a corresponding system of coupled non-linear equations for both continuum electrostatics with a uniform dielectric constant, and a structured solvent—a dipolar Coulomb fluid—including non-local effects. While the approach is only approximate and also limited to corrections in the so-called weak fluctuation regime, it allows us to include physically relevant effects, as we show for a range of applications of these equations.

Keywords: electrostatics, self-consistent theory, correlation effects

(Some figures may appear in colour only in the online journal)

## 1. Introduction

Poisson–Boltzmann (PB) theory is the cornerstone of soft matter electrostatics, but in recent years several shortcomings of this theory have also been clearly revealed. PB theory is a mean-field theory, hence it neglects all fluctuation or correlation effects, and as a simple continuum theory it also ignores the structure of solvents and ions. In the presence of ions of high valency, prominent in biological systems in particular, the theory even fails qualitatively. A systematic field-theoretic approach to soft matter electrostatics developed with the counter-ion case has allowed the identification of a coupling parameter [1],

$$\Xi \equiv \frac{q^3|\sigma|e^4\beta^2}{8\pi\varepsilon^2} = q^2\frac{\ell_B}{\ell_{CG}} \qquad (1)$$

where $q$ is the valency of the counter-ions, $\sigma e$ is the surface charge density with the electronic charge $e$, $\varepsilon$ is the dielectric constant, and $\beta = 1/k_BT$. $\Xi$ is thus essentially the ratio of the Bjerrum length $\ell_B = e^2/(4\pi\varepsilon_0\varepsilon_w k_BT)$ and the Gouy–Chapman length $\ell_{GC} = 1/(2\pi\ell_B q|\sigma_s|)$. Poisson–Boltzmann theory is the weak coupling limit $\Xi \to 0$ of the more general theory, while for $\Xi \to \infty$, the strong coupling case, a single-particle picture emerges [2].

Even within the weak coupling limit, or for intermediate values of the coupling parameter, Poisson–Boltzmann theory does not fully describe the electrostatic phenomena in soft matter systems. Being a mean-field theory, it entirely lacks the correlation effects between the charges. These are, however, crucial in many physical settings. For the case of electrostatics near macromolecular surfaces or membrane interfaces—one

of the most basic situations encountered in soft matter—this omission does not allow the image charge effects of solvated ions to be treated. Another crucial effect is the charge reversal of macromolecules induced by the overscreening of their bare charge by multivalent counter-ions. This effect can indeed modify the interactions between charged objects, even in a qualitative way.

Therefore, in order to remedy this deficit, methods to include fluctuation effects have been devised. In this topical review, we deal exclusively with one such approach, which relies on a variational formalism, leading to self-consistently coupled equations of the electrostatic potential and its correlation function. The formulation that we base this on was originally introduced by Netz and Orland [3], following earlier work by Avdeev *et al* [4]. More precisely, Netz and Orland used the variational approach to calculate the mean-field level charge renormalization associated with the non-linearity of the Poisson–Boltzmann approach, without considering the correlation effects embodied in the self-consistent equations.

In recent years, the variational approach has, however, seen a number of physically relevant applications, covering different charge geometries, and even dynamical situations such as flow-related effects in nanopores. Hatlo *et al* considered the variational formulation of inhomogeneous electrolytes by introducing a restricted self-consistent scheme [5]. In [6, 7], one of us (SB) introduced a numerical scheme for the exact solution of the variational equations in slit and cylindrical nanopores. At this point, we should also mention the one-loop treatment of charge correlations that allows the analytical treatment of inhomogeneous electrolytes. Netz introduced the one-loop calculation of the ion partition at membrane surfaces in counter-ion-only liquids [8]. This was subsequently extended by Lau [9] to electrolytes symmetrically partitioned around a thin charged plane. In [6], we integrated the one-loop equations of a charged liquid in contact with a thick dielectric membrane. Finally, in [10, 11], we considered the role played by charge correlations on the electrophoretic and pressure-driven DNA translocation through nanopores.

In addition, while the original self-consistent equations only covered the case of systems that can be described by macroscopic dielectric constants, modified equations have been derived that can also include the effects from fluid structure. The first dipolar Poisson–Boltzmann theory including solvent molecules as point-dipoles was introduced in [12]. Abrashkin *et al* incorporated excluded volume effects into this model [13]. One of us (SB) derived a Poisson–Boltzmann equation that relaxes the point-dipole approximation and includes solvent molecules as finitely sized dipoles [14]. This model, which also accounts for ionic polarizability, was shown to contain the non-locality of electrostatic interactions observed in molecular dynamics simulations. Finally, we derived the dipolar self-consistent equations of this model, and in this way generalized Netz–Orland's variational equations for explicit solvent liquids [15].

Our ambition in this topical review is to provide a quick technical introduction to the method and the results that have been achieved with this approach. We have attempted to make this approach accessible to newcomers by giving a sufficient amount of technical detail for the simpler cases. This level of detail then, by necessity, diminishes for the more complex ones that follow; however, we hope that by that time, a reader willing to go through about the first third of the equations in a stepwise manner will have no difficulty in following the rest of the paper. For the latter part, as in all reviews, we refer our readers to the original articles for further details.

The material presented in the review is organized as follows. In section 2 we derive the model equations which have been called either variational PB equations, self-consistent field equations, or fluctuation-enhanced Poisson–Boltzmann equations (FE-PB), for the case of a system with 1–1 salt. We also discuss the limits of validity that can be expected from the equations. In section 3 we review the results for systems whose dielectric properties can be properly covered by dielectric constants. In particular, we discuss situations of high current interest involving the application of the approach to nanopore geometries. Section 4 contains very recent extensions of the approach, including the fluctuation-enhanced Poisson–Boltzmann equations for a dipolar solvent, the DPBL-equation, as well as a non-local version of the latter. Section 5 presents a brief summary and outlook. We finally note that we explain, wherever possible at present, the theoretical results closely in relation to the experimental findings. This is obviously the ultimate way to validate a theory, and the reader is invited to see how far the self-consistent approach to soft matter electrostatics has been carried so far.

## 2. Fluctuation-enhanced Poisson–Boltzmann equations

### 2.1. Derivation

The fluctuation-enhanced Poisson–Boltzmann equations result from the observation that a simple perturbative treatment of the non-linear Poisson–Boltzmann equation only has poor convergence properties. This is particularly the case for electrolytes in contact with low permittivity macromolecules or membranes where the singularity of the resulting image-charge potential does not allow the one-loop expansion of the grand potential. As in many other branches of physics, variational approaches thus come as an often fruitful alternative. In this vein, the starting point is the Gibbs variational procedure that consists of extremizing the variational grand potential in the form [3] $\Omega_v = \Omega_0 + \langle H - H_0 \rangle_0 / \Xi$, where $H_0[\phi]$ is a trial Hamiltonian functional and the bracket $\langle \cdot \rangle_0$ denotes the field-theoretic average with respect to this Hamiltonian. For this Hamiltonian, the most general functional ansatz is a Gaussian one including the mean electrostatic potential $\Phi$ and the covariance of the field expressed via its Green's function $G$ as variational parameters

$$H_0[\phi] = \frac{1}{2} \int_{\mathbf{r}} \int_{\mathbf{r}'} [\phi(\mathbf{r}) + i\Phi(\mathbf{r})](\Xi G(\mathbf{r}, \mathbf{r}'))^{-1}[\phi(\mathbf{r}') + i\Phi(\mathbf{r}')]. \quad (2)$$

For definiteness, we now consider the case of monovalent ions with charges $\pm q$ confined to a region $\Omega$ in the presence of a fixed charge density $\varrho_f$. The Hamiltonian is then, following [16]

$$H[\phi] = \frac{1}{2\pi} \int_r \left[ \frac{(\nabla\phi)^2}{2} + i\varrho_f\phi - \frac{\Lambda}{2} e^{\Xi G_0(\mathbf{r},\mathbf{r})/2} \cos\phi \right], \qquad (3)$$

where $\Lambda$ is the fugacity of the ions, and $G_0(\mathbf{r},\mathbf{r}') = 1/|\mathbf{r} - \mathbf{r}'|$ is the bare Coulomb potential. The introduction of $G_0$ at this level takes care of the regularization of the Green's function $G(\mathbf{r},\mathbf{r}')$ in the final equations as the ionic self-energy corresponding to the equal-point correlation function $G(\mathbf{r},\mathbf{r})$ diverges in the present dielectric continuum formalism. In equation (3), this factor shifts the chemical potential of the ions. With this ansatz, we can compute the grand potential $\Omega_v$ from which the sought equations follow after extremization with respect to the functions $\Phi$ and $G$. These self-consistent equations read as

$$\nabla^2\Phi(\mathbf{r}) - \Lambda e^{-\Xi c(\mathbf{r})/2} \sinh\Phi(\mathbf{r}) = -2\varrho_f(\mathbf{r}), \qquad (4)$$

$$[\nabla^2 - \Lambda e^{-\Xi c(\mathbf{r})/2} \cosh\Phi(\mathbf{r})]G(\mathbf{r},\mathbf{r}') = -4\pi\delta(\mathbf{r} - \mathbf{r}'), \qquad (5)$$

$$c(\mathbf{r}) = \lim_{\mathbf{r}\to\mathbf{r}'}[G(\mathbf{r},\mathbf{r}') - G_0(\mathbf{r},\mathbf{r}')]. \qquad (6)$$

Equation (4) is a modified Poisson–Boltzmann equation, augmented by the correlation function (6) in the exponential. The correlation function fulfills a modified Debye–Hückel (DH) equation, equation (5), in which the usual inverse Debye-length $\kappa^2$ is replaced by a non-linear function of both $c(\mathbf{r})$ and $\phi(\mathbf{r})$. These equations are one realization (for the case of 1–1 salt, and without further specification of the fixed charge geometries) of the self-consistent or fluctuation-enhanced Poisson–Boltzmann equations. One should also note that equations (4) and (5) can be easily generalized to an asymmetrical electrolyte (see e.g. [7]).

## 2.2. Validity

The self-consistent equations (4)–(6) are, by their very construction, only approximate. Their validity ultimately rests on the validity of the Gaussian assumption to begin with, and this is, as usual in variational approaches, not always easy to quantify. One can, however, identify the validity regime qualitatively by considering the charge correlations in a bulk electrolyte. In this case, the electrostatic potential $\phi$ vanishes and we are left with a Debye–Hückel type equation for the Green's function [17]

$$-\nabla^2 G(\mathbf{r},\mathbf{r}') + \Lambda e^{-\Xi c(\mathbf{r})/2} G(\mathbf{r},\mathbf{r}') = 4\pi\delta(\mathbf{r} - \mathbf{r}'). \qquad (7)$$

If we define the screening parameter as $\kappa^2 \equiv \Lambda e^{-\Xi c(\mathbf{r})/2}$, the Green's function becomes

$$G(\mathbf{r},\mathbf{r}') = \frac{e^{-\kappa|\mathbf{r} - \mathbf{r}'|}}{|\mathbf{r} - \mathbf{r}'|}. \qquad (8)$$

Inserting equation (8) into equation (6), one finds $c = -\kappa$. We are thus led to a first self-consistency condition given by

$$\kappa^2 = \Lambda e^{\Xi\kappa/2}. \qquad (9)$$

This equation ceases to have a solution for large values of the coupling parameter $\Xi$, clearly indicating that the self-consistent equations (5) and (6) are only valid for weak to moderate charge correlations. This condition can be, in turn, quantified through equation (1) in terms of the model parameters.

In inhomogeneous liquids, the validity limit of the self-consistent equations (5) and (6) is not so easy to assess, as they are, due to their highly non-linear character, not amenable to analytic solutions, even for simple geometries. Numerical methods have recently been developed to solve them [6, 7, 16, 18]. In particular, in comparison with the MC simulations, [6] and [7] identified the validity regime of the equations for liquids confined to slit and cylindrical nanopores, respectively. In the following we will discuss the approximate solutions of equations (4)–(6) and their modifications to physically relevant situations, which to some extent also permit analytical calculations. In particular, we confront these solutions with data from experiments and simulations.

## 3. The variational equations for a dielectric continuum

In this section, we turn to the application of the SC equations to some specific physical situations. First, we discuss ion correlations and charge reversal at a planar interface, and then move on to the dynamic effects associated with DNA translocation through membrane pores. These examples were selected as they allow us to convey the main insights about correlation effects that can be gained from the variational approach, and in conjunction with ions of higher valency, where PB-theory is known to fail. Further applications of the equations in the case of a dielectric continuum concern the effect of image charges on macro-ions [19] and on the electrical double layer [20, 21]. The ion size effects upon ionic exclusion from dielectric interfaces and slit nanopores were treated in [22–24]. The modification of ion polarizabilities from the gas phase to solvation in polar liquids was discussed in [25].

### 3.1. One-loop expansion of the SC equations and charge reversal

We begin the discussion with the one-loop (1-$\ell$) expansion of the electrostatic SC equations, valid exclusively for dielectrically continuous systems $\varepsilon(\mathbf{r}) = \varepsilon_w$. We consider a symmetric electrolyte composed of two ionic species with valencies $\pm q$ and a bulk density $\rho_b$. In order to facilitate the link to the research literature, in passing from equation (4) to the subsequent equation (10) we will introduce the definition of the new average potential $\psi(\mathbf{r}) = -q\Phi(\mathbf{r})$ and the Green's function $v(\mathbf{r},\mathbf{r}') = \Xi G(\mathbf{r},\mathbf{r}')$. For this case, the SC equations read as

$$\nabla^2\psi(\mathbf{r}) - \kappa_b^2 e^{-V_w(\mathbf{r}) - \frac{q^2}{2}\delta v(\mathbf{r},\mathbf{r})} \sinh[\psi(\mathbf{r})] = -4\pi\ell_B q\sigma(\mathbf{r}) \qquad (10)$$

$$\nabla^2 v(\mathbf{r},\mathbf{r}') - \kappa_b^2 e^{-V_w(\mathbf{r}) - \frac{q^2}{2}\delta v(\mathbf{r},\mathbf{r})} \cosh[\psi(\mathbf{r})]v(\mathbf{r},\mathbf{r}')$$
$$= -4\pi\ell_B\delta(\mathbf{r} - \mathbf{r}'), \qquad (11)$$

where the ionic self-energy (or renormalized equal-point correlation function) is defined by

$$\delta v(\mathbf{r}) \equiv \delta v(\mathbf{r}, \mathbf{r}) = \ell_B \kappa_b + v(\mathbf{r}, \mathbf{r}) - v_c^b(0), \qquad (12)$$

where the DH screening parameter $\kappa_b^2 = 8\pi \ell_B q^2$, and the function $V_w(\mathbf{r})$ is the ionic steric potential accounting for the rigid boundaries in the system.

The 1-$\ell$ expansion of these equations consists of Taylor-expanding equations (10) and (11) in terms of the electrostatic Green's function $v(\mathbf{r}, \mathbf{r}')$. Splitting the average potential into its MF and 1-$\ell$ components as $\psi(\mathbf{r}) = \psi_0(\mathbf{r}) + \psi_1(\mathbf{r})$, for the MF potential and the 1-$\ell$ electrostatic Green's function equations one obtains

$$\nabla^2 \psi_0(\mathbf{r}) - \kappa_b^2 e^{-V_w(\mathbf{r})} \sinh[\psi_0(\mathbf{r})] = -4\pi \ell_B \sigma(\mathbf{r}) \quad (13)$$

$$\{\nabla^2 - \kappa_b^2 e^{-V_w(\mathbf{r})} \cosh[\psi_0(\mathbf{r})]\} v(\mathbf{r}, \mathbf{r}') = -4\pi \ell_B \delta(\mathbf{r} - \mathbf{r}'), \qquad (14)$$

and for the 1-$\ell$ correction to the average potential

$$\{\nabla^2 - \kappa_b^2 e^{-V_w(\mathbf{r})} \cosh[\psi_0(\mathbf{r})]\} \psi_1(\mathbf{r}) = -\frac{q^2}{2} \kappa_b^2 e^{-V_w(\mathbf{r})} \delta v(\mathbf{r}) \sinh[\psi_0(\mathbf{r})]. \qquad (15)$$

In order to solve the system of differential equations (13)–(15), we first invert equation (14) and recast it in a more practical form for analytical evaluation. By using the definition of the Green's function

$$\int d\mathbf{r}_1 v^{-1}(\mathbf{r}, \mathbf{r}_1) v(\mathbf{r}_1, \mathbf{r}') = \delta(\mathbf{r} - \mathbf{r}'), \qquad (16)$$

one can invert equation (14) and express the electrostatic kernel as

$$v^{-1}(\mathbf{r}, \mathbf{r}') = -\frac{1}{4\pi \ell_B} \{\nabla_{\mathbf{r}}^2 - \kappa_b^2 e^{-V_w(\mathbf{r})} \cosh[\psi_0(\mathbf{r})]\} \delta(\mathbf{r} - \mathbf{r}'), \qquad (17)$$

in terms of which equation (15) can be written as

$$\int d\mathbf{r}_1 v^{-1}(\mathbf{r}_2, \mathbf{r}_1) \psi_1(\mathbf{r}_1) = q^4 \rho_b e^{-V_w(\mathbf{r}_2)} \delta v(\mathbf{r}_2) \sinh[\psi_0(\mathbf{r}_2)]. \quad (18)$$

Multiplying equation (18) with the potential $v(\mathbf{r}, \mathbf{r}_2)$ and integrating over the variable $\mathbf{r}_2$, one finally gets the integral relation for the 1-$\ell$ potential correction completing the equations (13) and (14)

$$\psi_1(\mathbf{r}) = \rho_b q^4 \int d\mathbf{r}_1 e^{-V_w(\mathbf{r}_1)} v(\mathbf{r}, \mathbf{r}_1) \delta v(\mathbf{r}_1) \sinh[\psi_0(\mathbf{r}_1)]. \qquad (19)$$

We also note that within 1-$\ell$-theory, the ion number densities are given by

$$\rho_{\pm}(\mathbf{r}) = \rho_b e^{-V_w(\mathbf{r}) \mp \psi_0(\mathbf{r})} \left\{1 - \frac{q^2}{2} \delta v(\mathbf{r}) \mp \psi_1(\mathbf{r})\right\}. \qquad (20)$$

We now have the main set of equations ready and turn to the analytical solutions of equations (13)–(15) for a simple planar geometry in order to investigate the charge inversion phenomenon [7]. Then we will couple these equations with the Stokes equation and show that charge inversion gives rise to a reversal of electrophoretic DNA mobility [10] and hydrodynamically induced ion currents through cylindrical pores [11].

*3.1.1. Ionic correlations and charge reversal at planar interfaces.* In this part, we consider the charge reversal effect

in the case of a negatively charged planar interface located at $z = 0$. The electrolyte occupies the half-space $z > 0$ while the left half-space at $z < 0$ is ion-free. In the SC-equations this corresponds to a steric potential $V_w(\mathbf{r}) = \infty$ if $z < 0$ and $V_w(\mathbf{r}) = 0$ for $z > 0$. The wall charge distribution function is $\sigma(\mathbf{r}) = -\sigma_s \delta(z)$. By introducing the Gouy–Chapman length $\ell_{GC} \equiv \mu = 1/(2\pi q \ell_B \sigma_s)$ that corresponds to the thickness of the interfacial counter-ion layer, the solution of equation (13) satisfying Gauss's law $\psi_0'(z = 0) = 2/\mu$ reads as

$$\psi_0(z) = -2 \ln\left[\frac{1 + e^{-\kappa_b(z+z_0)}}{1 - e^{-\kappa_b(z+z_0)}}\right], \qquad (21)$$

where we introduced the parameter $s = \kappa_b \mu$ and the auxiliary functions $z_0 = -\ln[\gamma(s)]/\kappa_b$ and $\gamma(s) = \sqrt{s^2 + 1} - 1$. In the DH-limit of a weak surface charge or strong salt, the potential (21) becomes $\psi_0(z) \simeq (2/s) e^{-\kappa_b z}$. The parameter $s$ thus corresponds to the inverse magnitude of the surface potential.

Taking advantage of the planar symmetry in the $(x, y)$-plane one can expand the Green's function in the Fourier basis as

$$v(\mathbf{r}, \mathbf{r}') = \int_0^\infty \frac{dk\, k}{2\pi} J_0(k|\mathbf{r}_\parallel - \mathbf{r}'_\parallel|) \tilde{v}_0(z, z'), \qquad (22)$$

where $\mathbf{r}_\parallel$ is the position vector in the $(x, y)$-plane and $J_0$ is a Bessel function of the order zero. Substituting the expansion (22) together with the MF-potential (21) into the kernel equation (11), the latter takes the form

$$\partial_z^2 [1 - \theta(z)\{p_b^2 + 2\kappa_b^2 \text{csch}^2[\kappa_b(z+z_0)]\}] \tilde{v}(z, z', k)$$
$$= -4\pi \ell_B \delta(z - z') \qquad (23)$$

where we defined the function $p_b = \sqrt{k^2 + \kappa_b^2}$. The solution of equation (23), satisfying the continuity of the potential $\tilde{v}(z, z')$ and the displacement field $\partial_z \tilde{v}(z, z')$ at $z = 0$ and $z = z'$ reads

$$\tilde{v}_0(z, z') = \frac{2\pi \ell_B p_b}{k^2} [h_+(z) h_-(z') + \Delta h_-(z) h_-(z')] \quad (24)$$

for $0 \leqslant z \leqslant z'$, where the homogeneous solutions of equation (23) are given by

$$h_\pm(z) = e^{\pm p_b z} \left\{1 \mp \frac{\kappa_b}{p_b} \coth[\kappa_b(z+z_0)]\right\}, \qquad (25)$$

and the $\Delta$-function reads

$$\Delta = \frac{\kappa_b^2 \text{csch}^2(\kappa_b z_0) + (p_b - k)[p_b - \kappa_b \coth(\kappa_b z_0)]}{\kappa_b^2 \text{csch}^2(\kappa_b z_0) + (p_b + k)[p_b + \kappa_b \coth(\kappa_b z_0)]}. \qquad (26)$$

For $z \geqslant z'$, the solution of equation (23) can be obtained by interchanging the variables $z$ and $z'$ in equation (24). From now on we switch to the non-dimensionalized coordinate $\bar{z} = \kappa_b z$. Rescaling the wave-vector of the Fourier expansion (22) as $k \to u = p_b/\kappa_b$ as well, and inserting the function (24) into equation (12), the ionic self-energy accounting for the charge correlations takes the form

$$\delta v_0(\bar{z}) = \Gamma \int_1^\infty \frac{du}{u^2 - 1} \{-\text{csch}^2[\bar{z} - \ln \gamma_c(s)]$$
$$+ \bar{\Delta}(u + \coth[\bar{z} - \ln \gamma_c(s)])^2 e^{-2\bar{z}u}\}, \qquad (27)$$

where we defined the electrostatic coupling parameter $\Gamma = \ell_B \kappa_b$ and

$$\bar{\Delta} = \frac{1 + s(su - \sqrt{s^2 + 1})(u - \sqrt{u^2 - 1})}{1 + s(su + \sqrt{s^2 + 1})(u + \sqrt{u^2 - 1})}. \qquad (28)$$

Inserting the MF-potential (21), the Green's function (24) and the self-energy (27) into equation (19), and carrying out the spatial integral, the 1-$\ell$-correction to the average potential takes the form

$$\psi_{1\ell}(\bar{z}) = \frac{q^2}{4}\Gamma\,\mathrm{csch}\,[\bar{z} - \ln\gamma_c(s)]\int_1^\infty \frac{\mathrm{d}u}{u^2 - 1}F(\bar{z}, u), \qquad (29)$$

where we introduced the auxiliary function

$$F(\bar{z}, u) = \frac{2 + s^2}{s\sqrt{1 + s^2}} - \bar{\Delta}\left(\frac{1}{u} + 2u + \frac{2 + 3s^2}{s\sqrt{1 + s^2}}\right)$$
$$+ \frac{\bar{\Delta}}{u}e^{-2u\bar{z}} + (\bar{\Delta}e^{-2u\bar{z}} - 1)\coth[\bar{z} - \ln\gamma_c(s)]. \qquad (30)$$

We note that the correlation-corrected ion densities (20) are fully characterized by the potentials (21), (27) and (29). One also sees that these functions depend solely on the parameters $s$ and $\Gamma$.

In figure 1, we show the 1-$\ell$-correction to the ion densities

$$\Delta\rho_\pm(\bar{z}) \equiv \frac{\rho_\pm(\bar{z}) - \rho_\pm^{MF}(\bar{z})}{\rho_\pm^{MF}(\bar{z})} = -\frac{q^2}{2}\delta v_0(\bar{z}) \mp \psi_{1\ell}(\bar{z}), \qquad (31)$$

where the MF-ion densities are given by $\rho_\pm^{MF}(\bar{z}) = \rho_b e^{\mp\psi_0(\bar{z})}$. The top plot (a) illustrates the density correction at a weakly charged membrane ($s = 1000$). In this case, the absence of ions in the left half-space results in an ionic screening deficiency close to the membrane surface. As a result, ions prefer to move away from the interface towards the bulk where they are more efficiently screened and possess a lower free energy. This translates in turn into a positive ionic self-energy $\delta v_0(\bar{z}) > 0$ (see inset) and a decrease in the MF-level co-ion and counter-ion densities (main plot) by the charge correlations.

In the plot of figure 1(b), we consider a strongly charged membrane ($s = 0.75$). In this parameter regime, the strong counter-ion attraction results in an interfacial charge excess. The ions being more efficiently screened in the vicinity of the membrane surface, they tend to approach the interface. This effect is reflected in the attractive ionic self-energy $\delta v_0(\bar{z}) < 0$ (inset) and the amplification of the MF-density of both co-ions and counter-ions (main plot). In [6], it was shown that the transition between these two regimes with the surface self-energy $\delta v_0(0)$ switching from positive to negative occurs when the size of the interfacial counter-ion layer becomes comparable to the ionic screening radius in the bulk region, i.e. at $\mu \simeq \kappa_b^{-1}$. This equality yields the characteristic membrane charge $\sigma_s^* = \sqrt{2\rho_b/(\pi\ell_B)}$ above which the interfacial screening dominates the bulk screening.

For a negatively charged membrane, the MF-potential is negative (see equation (18)). Furthermore, in the inset of
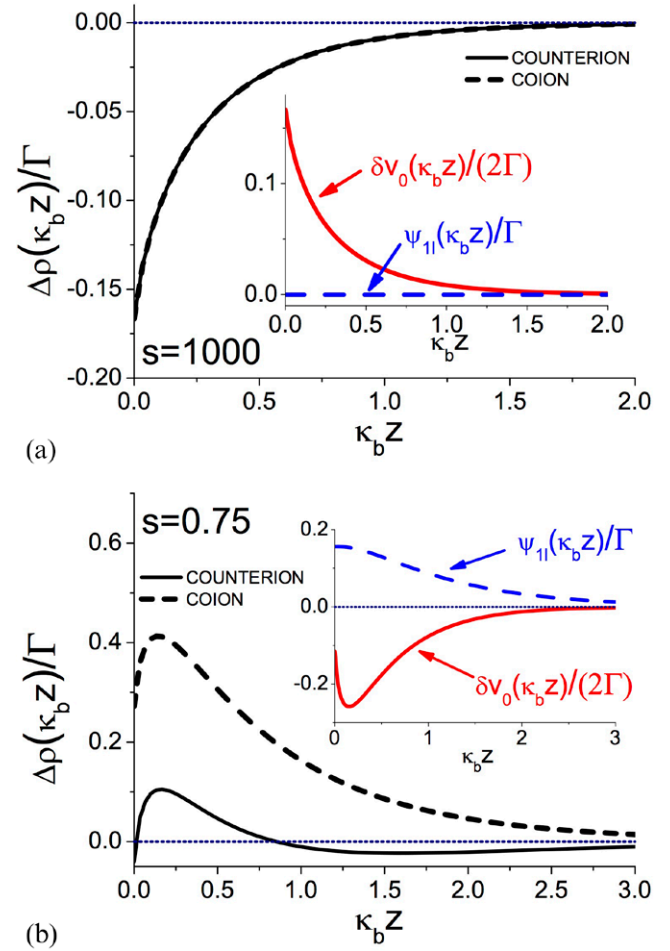


**Figure 1.** One-loop corrections to the counter-ion (solid lines) and co-ion densities (dashed lines) from equation (31), for two different values of the parameter $s = \kappa_b\mu$, the ratio of the Gouy–Chapman and the screening length. Case (a): $s = 1000$ (a weakly charged membrane) and case (b): $s = 0.75$ (a strongly charged membrane). The inset shows the ionic self-energy and the one-loop correction to the external potential for these parameters.

figure 1(b) where we plotted the 1-$\ell$-correction equation (29) to the average potential, one sees that the former is positive. This stems from the interfacial screening excess. Thus, at strongly charged membranes, correlations attenuate the magnitude of the negative MF-potential.

We will now show that this peculiarity is the precursor of the *charge reversal* effect. In order to illustrate this point, we note that at large distances from the charged plane $\bar{z} \gg 1$, the MF-potential (21) behaves as $\psi_0(\bar{z}) \simeq -4\gamma(s)e^{-\bar{z}}$. Expanding the 1-$\ell$-correction to the average electrostatic potential (30) in the same limit, one finds that the correlation-corrected average potential $\psi_{1\ell}(\bar{z}) = \psi_0(\bar{z}) + \psi_1(\bar{z})$ takes the form

$$\psi_{1l}(\bar{z}) \simeq -\frac{2}{s}\eta(s)e^{-\bar{z}}, \qquad (32)$$

where we introduced the charge renormalization factor accounting for electrostatic many-body effects

$$\eta(s) = 2s\gamma(s)\left[1 - \frac{q^2\Gamma}{8}\,I(s)\right], \qquad (33)$$
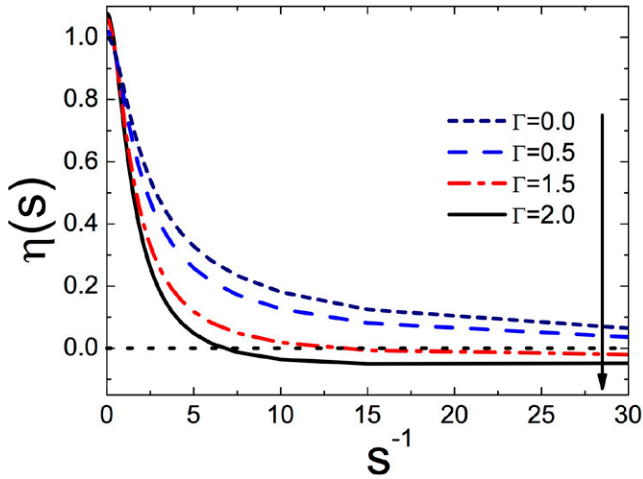
**Figure 2.** Charge renormalization factor $\eta(s)$, see equation (33) against $s^{-1}$, $s = \kappa_b \mu$, for several values of the coupling parameter $\Gamma = \ell_B \kappa_b$.

with the auxiliary function

$$I(s) = \int_1^\infty \frac{du}{u^2 - 1} \left\{ \frac{2 + s^2}{s\sqrt{1 + s^2}} - 1 - \bar{\Delta} \left( \frac{1}{u} + 2u + \frac{2 + 3s^2}{s\sqrt{1 + s^2}} \right) \right\}. \tag{34}$$

In figure 2, we plot equation (33) versus $s^{-1}$ for various coupling parameters $\Gamma$. In the MF-limit $\Gamma = 0$, and the charge renormalization factor $\eta(s)$ accounts for the non-linearities neglected by the linearized PB-theory. As the latter overestimates the actual value of the electrostatic potential at strong charges, with an increasing surface charge from left to right, the correction factor $\eta(s)$ drops from unity to zero. Moreover, one sees that at the coupling parameter $\Gamma = 2$, the charge renormalization factor passes from positive to negative. In other words, at large distances from the interface, the total average potential (32) switches from negative to positive. This is the signature of the *charge inversion* effect. As the adsorbed counter-ions overcompensate for the negative fixed surface charge, the interface acquires an effective positive charge. For small $s$ (or large surface charge density), equation (33) takes the asymptotic form

$$\eta(s) = 2s \left[ 1 - \Gamma \frac{\pi - 4\ln(2s)}{16} \right] + O(s^2). \tag{35}$$

Setting the equality (35) to zero, one finds that the charge reversal takes place at the particular value

$$s_c(\Gamma) = \frac{1}{2} \exp \left( \frac{\pi}{4} - \frac{4}{\Gamma} \right). \tag{36}$$

Having established the charge reversal effect in the planar geometry, we will now turn to its influence on ion currents and polymer mobilities through cylindrical nanopores, which is a problem of current interest in the field of soft matter physics.

*3.1.2. Electrophoretic DNA mobility reversal by multivalent counter-ions.* In this part we discuss the effect of charge inversion induced by multivalent ions on the electrophoretic mobility of a DNA molecule [10]. The molecule is modelled

as a charged cylinder with a radius of $a = 1$ nm, translocating through a nanopore of cylindrical geometry with a radius of $d = 3$ nm. The configuration is depicted in figure 3. The solution of the 1-$\ell$ equations (13)–(15) in a cylindrical geometry is similar to their solution in planar geometry. Thus, we will skip the technical details here and refer to [7] and [10] for details. The DNA molecule has a negative surface charge distribution $\sigma(r) = -\sigma_p \delta(r - a)$, with $\sigma_p = 0.4$ e/nm$^2$ and $r$ being the radial distance of ions from the symmetry axis of the cylindrical polymer. In the general case, the permittivity of the nanopore $\varepsilon_m$ and DNA may differ from the water permittivity $\varepsilon_w$. However, in order to simplify the technical task, we assume that there is no dielectric discontinuity in the system and set $\varepsilon_m = \varepsilon_p = \varepsilon_w = 80$.

As the electrophoretic translocation of DNA under an external potential gradient $\Delta V$ corresponds to the collective motion of the electrolyte and the DNA molecule, first we need to derive the convective fluid velocity $u_c(r)$ given by the Stokes equation

$$\eta \nabla^2 u_c(r) + e\rho_c(r) \frac{\Delta V}{L} = 0, \tag{37}$$

with the viscosity coefficient of water $\eta = 8.91 \times 10^{-4}$ Pa · s, the nanopore length $L$, and the liquid charge density

$$\rho_c(r) = \sum_i q_i \rho_i(r), \tag{38}$$

where $\rho_i(r)$ is the number density of the ionic species $i$ with valency $q_i$,

$$\rho_i(r) = \rho_{ib} e^{-q_i \psi_0(r)} \left[ 1 - q_i \psi_1(r) - \frac{q_i^2}{2} \delta v(r) \right]. \tag{39}$$

By making use of the Poisson equation $\nabla^2 \psi_{1\ell}(r) + 4\pi \ell_B \rho_c(r) = 0$ in equation (37), the latter can be written explicitly in the cylindrical geometry as

$$\frac{\eta}{r} \frac{\partial}{\partial r} r \frac{\partial}{\partial r} u_c(r) - \frac{k_B T}{er} \frac{\Delta V}{L} \frac{\partial}{\partial r} r\varepsilon(r) \frac{\partial}{\partial r} \psi_{1\ell}(r) = 0. \tag{40}$$

In order to solve equation (40), we first note that the 1-$\ell$-potential $\psi_{1\ell}(r)$ satisfies Gauss's law $\phi'(a) = 4\pi \ell_B \sigma_p$ at the DNA surface. In the steady-state regime, where DNA translocates at a constant velocity $v$, the longitudinal electric force per polymer length $F_e = -2\pi a e \sigma_p \Delta V/L$ will compensate for the viscous friction force $F_v = 2\pi a \eta u_c'(a)$, that is $F_e + F_v = 0$. Finally, we impose the boundary conditions $u_c(d) = 0$ (no-slip) and $u_c(a) = v$. Integrating equation (40) and imposing the above-mentioned conditions, we get the convective flow velocity

$$u_c(r) = -\mu_e \frac{\Delta V}{L} \left[ \phi(d) - \phi(r) \right], \tag{41}$$

and the DNA translocation velocity

$$v = -\mu_e \frac{\Delta V}{L} \left[ \phi(d) - \phi(a) \right], \tag{42}$$

with the reduced electrophoretic mobility

$$\mu_e = \frac{k_B T \varepsilon_w}{e\eta}. \tag{43}$$

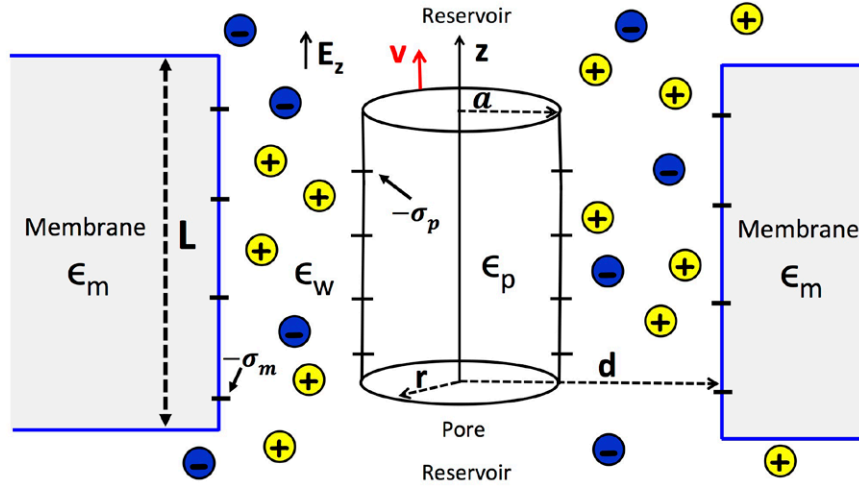**Figure 3.** Nanopore geometry: a cylindrical polyelectrolyte of radius $a = 1$ nm, surface charge $-\sigma_p$, and dielectric permittivity $\varepsilon_p$ is confined to a cylindrical pore of radius $d = 3$ nm, with wall charge $-\sigma_m$, and membrane permittivity $\varepsilon_m$. The permittivity of the electrolyte is $\varepsilon_w = 80$.

We now consider an electrolyte mixture of composition $KCl + ICl_m$ including an arbitrary type of multivalent counter-ion $I^{m+}$. The electrophoretic DNA velocity (42) against the multivalent ion density $\rho_{mb}$ is displayed in figure 4 for various multivalent ion types. With divalent $Mg^{2+}$ ions, the DNA translocation velocity is negative. This corresponds qualitatively to the classical MF-transport where the negatively charged DNA molecule moves in an opposite way to the applied electric field. However, in the mixed electrolytes containing trivalent spermidine and quadrivalent spermine ions, and with the increase of the multivalent ion density, the DNA velocity switches from negative to positive. In other words, at large multivalent counter-ion concentrations, the molecule translocates parallel with the field. Finally, one notes that beyond the mobility reversal density, the positive DNA velocity in spermidine and spermine liquids reaches a peak and drops beyond this point.

In order to explain the reversal of DNA mobility by multivalent counter-ions, in figure 5(a) we plot the cumulative charge density of the $KCl + Spm^{3+}Cl_3$ fluid including the polyelectrolyte charge

$$\rho_{\text{tot}}(r) = 2\pi \int_a^r dr' r' [\rho_c(r') + \sigma_s(r')] \quad (44)$$

for various bulk $Spd^{3+}$ concentrations. In figure 5(b), we also illustrate the cumulative liquid velocity (42) at the same densities. At the low $Spd^{3+}$ density $\rho_{3+b} = 2 \times 10^{-3}$ M, moving from the DNA surface towards the pore wall, the total charge density rises from the net DNA charge towards zero. This corresponds qualitatively to the MF-picture where counter-ions gradually screen the DNA charge. Hence, the negatively charged fluid and DNA move in an opposite way to the field, that is $u_c(r) < 0$ and $v = u_c(a) < 0$. Increasing now the $Spd^{3+}$ density to $\rho_{3+b} = 7 \times 10^{-3}$ M, the cumulative charge density switches from negative to positive at $r \gtrsim 1.3$ nm. This is the signature of charge reversal, where due to correlation effects induced by $Spd^{3+}$ ions, counter-ions locally overcompensate the DNA charge. Consequently, the liquid flows parallel
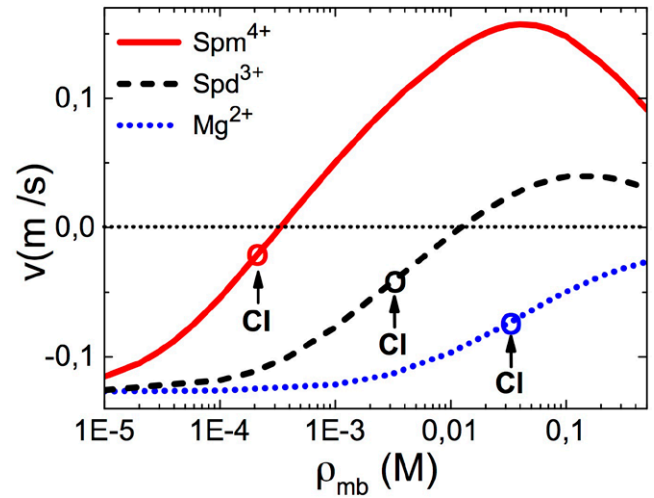


**Figure 4.** Polymer translocation velocity against the density of the multivalent counter-ion species $I^{m+}$ (see legend) in the electrolyte mixture $KCl + ICl_m$. The $K^+$ density is fixed at $\rho_{+b} = 0.1$ M. The confined double-stranded DNA has a surface charge of $\sigma_p = 0.4$ e nm$^{-2}$. The potential gradient is $\Delta V = 120$ mV. Circles mark the charge inversion (CI) point of the DNA molecule.

with the field ($u_c(r) > 0$) in the region $r > 1.3$ nm. However, because the hydrodynamic drag force is not sufficiently strong to dominate the electrostatic coupling between the DNA molecule and the external electric field, the molecule and the liquid around it continue to move in the direction of the field. At the higher $Spd^{3+}$ density $\rho_{3+b} = 1.2 \times 10^{-2}$ M, where charge reversal becomes more pronounced, the drag force compensates for the electric force on the DNA molecule exactly. As a result, the DNA stops its translocation, i.e. $v = u_c(a) = 0$. At higher $Spd^{3+}$ concentrations, the DNA molecule and the electrolyte move parallel with the field. We emphasize that an important challenge in DNA translocation consists of the extremization of the DNA translation velocity for an accurate sequencing of its genetic code [26]. The present result suggests that this can be achieved by tuning the trivalent or quadrivalent ion densities in the liquid.
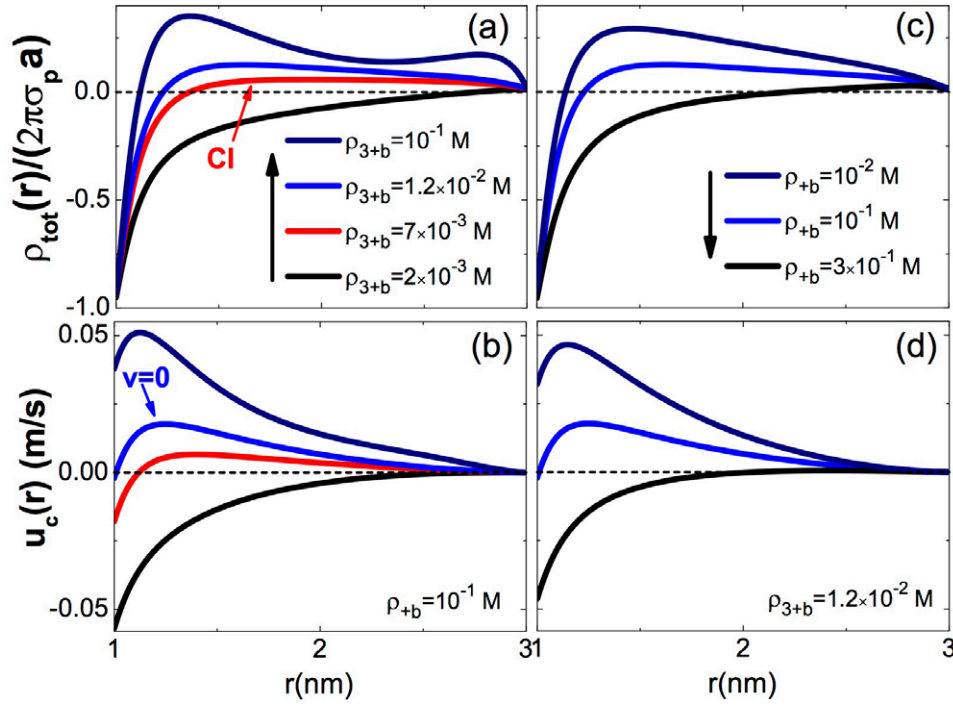
**Figure 5.** Cumulative charge densities rescaled with the bare DNA charge (top plots) and solvent velocities (bottom plots) at a fixed $K^+$ and a varying $Spd^{3+}$ concentration in (a) and (b), and a fixed $Spd^{3+}$ and a varying $K^+$ concentration in (c) and (d). In each column, the same colour in the top and bottom plots corresponds to a given bulk counter-ion concentration displayed in the legend. The remaining parameters are the same as in figure 4.

To summarize, it is found that the inversion of DNA mobility is induced by charge reversal. However, charge inversion should also be strong enough for mobility reversal to occur. This can also be seen in figure 4 where we display the charge inversion points with open circles. One notes that charge inversion precedes the mobility reversal that occurs only with trivalent and quadrivalent ions. We now focus on the peak of the velocity curves in this figure. One notes that at the highest $Spd^{3+}$ concentration in figure 5(a), the first positive peak of the cumulant charge density is followed by a well. The corresponding local drop of the cumulative charge density stems from the attraction of $Cl^-$ ions towards the charge-inverted DNA. At higher $Spd^{3+}$ concentrations, the stronger chloride attraction attenuates the charge reversal effect responsible for mobility inversion. This explains the reduction of the inverted charge mobility at high multivalent densities in figure 4. Finally, we consider the effect of potassium concentration that can easily be tuned in translocation experiments. In figures 5(c) and (d), we show the charge density and velocity at a fixed $Spd^{3+}$ concentration for various $K^+$ densities. Starting at the charge-inverted density values $\rho_{3+b} = 1.2 \times 10^{-2}$ M and $\rho_{+b} = 10^{-2}$ M, and raising the bulk potassium concentration from top to bottom, the cumulative charge density is seen to switch from positive to negative. This drives the DNA and electrolyte velocities from positive to negative. Thus, the $K^+$ ions cancel the DNA mobility inversion by weakening the charge reversal effect induced by ion correlations.

In the next paragraph, we will discuss the effect of charge reversal on the ion currents induced by a pressure gradient.

*3.1.3. Inversion of hydrodynamically induced ion currents through nanopores.* We now investigate the effect of charge correlations on streaming currents during hydrodynamically-induced polymer translocation events [11]. The DNA-membrane geometry, including the electrolyte mixture, is the same as in the previous section. The only difference is that in hydrodynamically-induced transport experiments, the externally applied voltage difference in figure 3 is replaced with a pressure gradient $\Delta P_z > 0$ at the pore edges. The resulting ionic current through the nanopore of length $L = 340$ nm and radius $d = 3$ nm is given by the number of charges flowing per unit time through the cross section of the channel,

$$I_{str} = 2\pi e \int_{a^*}^{d^*} \mathrm{d}r r \rho_c(r) u_s(r). \tag{45}$$

In equation (45), we introduced the effective pore and polymer radii $d^* = d - a_{st}$ and $a^* = a - a_{st}$ where $a_{st} = 2$ Å stands for the Stern layer accounting for the stagnant ion layer in the vicinity of the charged pore and DNA surfaces. The charge density function $\rho_c(r)$ is defined by equation (38). The streaming current velocity is given in turn by the solution of the Stokes equation with an applied pressure gradient

$$\eta \Delta u_s(r) + \frac{\Delta P_z}{L} = 0. \tag{46}$$

Solving equation (46), we impose the boundary conditions $u_s(d^*) = 0$ (no-slip) and $u_s(a^*) = v$. We also account for the fact that the viscous friction force $F_v = 2\pi a^* \eta u_s'(a^*)$ vanishes in the stationary state of the flow. Integrating equation (46)

under these conditions, the streaming flow velocity follows in the form of a Poisseuille profile,

$$u_s(r) = \frac{\Delta P_z}{4\eta L}\left[d^{*2} - r^2 + 2a^{*2}\ln\left(\frac{r}{d^*}\right)\right]. \qquad (47)$$

Knowledge of the charge density (38) and liquid velocity (47) completes the calculation of the ionic current of equation (45).

In figure 6(a), we report the streaming currents of the electrolyte mixture $KCl + ICl_m$ against the reservoir density of the multivalent cation species $I^{m+}$ in a neutral pore. At weak multivalent ion densities the current is positive. This corresponds to the MF-regime where the negatively charged translocating DNA attracts cations into the pore. Increasing the bulk magnesium concentration in the $KCl + MgCl_2$ liquid, in agreement with the MF ion transport picture, the streaming current drops slightly but remains positive. However, in the liquids containing spermidine and spermine ions, at a characteristic multivalent ion density, the current turns from positive to negative. It is noteworthy that this streaming current reversal has been previously observed in nanofluidic transport experiments through charged nanoslits without DNA [27].

The positive ion currents of figure 6(a), indicating a net negative charge flow through the pore, cannot be explained by MF-transport theory. In order to explain the underlying mechanism behind the current reversal, in figure 6(b) we plot the electrostatic cumulative charge density $\rho_{cum}(r) = 2\pi \int_a^r dr' r' \rho_c(r')$ and the hydrodynamic cumulative charge density $\rho_{cum}^*(r) = 2\pi \int_{a^*}^r dr' r' \rho_c(r')$ of the $KCl + SpdCl_3$ liquid normalized by the DNA charge. The hydrodynamic charge density only accounts for the mobile charges contributing to the streaming flow. Figure 6(c) displays the chloride densities between the DNA and pore surfaces. At the bulk spermidine concentration $\rho_{3+b} = 0.01$ M, figure 6(b) shows that the electrostatic cumulative charge density slightly exceeds the DNA charge. This is the sign of a DNA charge reversal effect. This in turn leads to a weak $Cl^-$ excess $\rho_-(r) > \rho_{-b}$ between the pore and the DNA (see figure 6(c)). However, because the charge reversal and the resulting chloride attraction is weak, the hydrodynamic flow charge dominated by the counter-ions is positive, i.e. $\rho_{cum}^* > 0$ for $a^* < r < d^*$. With an increase of the spermidine density to $\rho_{3+b} = 0.1$ M, where one arrives at the inverted current regime in figure 6(a), the intensified DNA charge reversal results in a much stronger $Cl^-$ attraction into the pore (see figures 6(b) and (c)). This strong anion excess leads in turn to a negative hydrodynamic charge density $\rho_{cum}(d) < 0$ and a negative streaming current through the pore.

To conclude, these calculations show that ionic current inversion during hydrodynamically induced DNA translocation events results from the anion excess in the pore induced in turn by the DNA charge reversal. It is important to note that, similar to the electrophoretic DNA transport of the previous section, the observation of streaming current reversal necessitates a strong DNA charge inversion for the adsorbed anions to bring the dominant contribution to the hydrodynamic flow. This is again illustrated in figure 6(a) where the charge
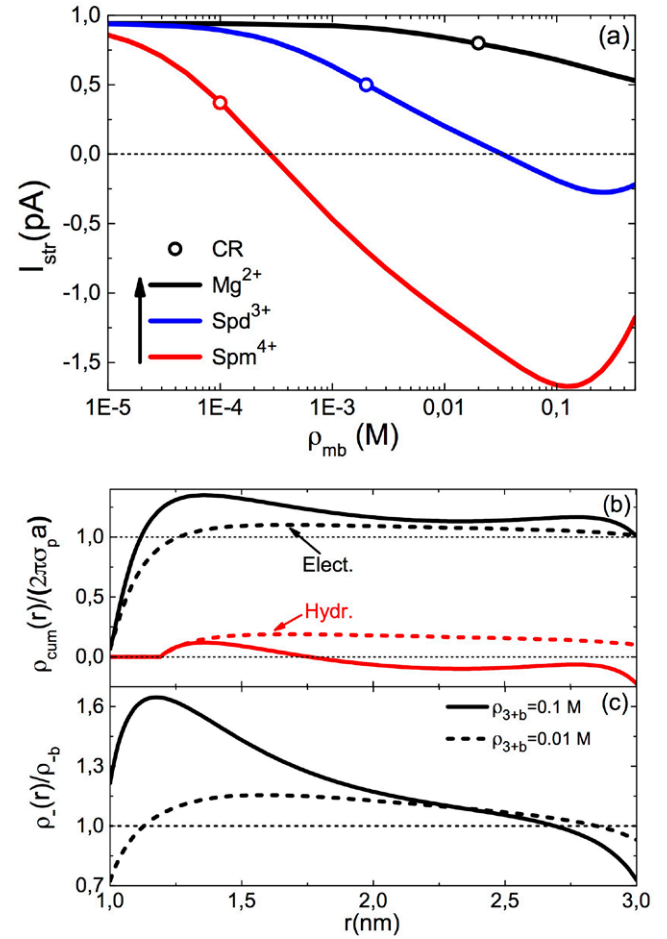


**Figure 6.** (a) Streaming current curves at a pressure gradient $\Delta P_z = 1$ bar against the reservoir density of the multivalent counterion species listed in the legend. Open circles mark the DNA charge reversal (CR) points. (b) Electrostatic (black curves) and hydrodynamic (red curves) cumulative charge densities, and (c) $Cl^-$ densities in the $KCl + SpdCl_3$ liquid at the reservoir concentrations $\rho_{3+b} = 0.01$ M (dashed curves) and 0.1 M (solid curves). The neutral nanopore ($\sigma_m = 0$) contains a double-stranded DNA molecule of charge density $\sigma_p = 0.4$ e nm$^{-2}$, with a bulk K$^+$ density $\rho_{+b} = 0.1$ M in all figures.

reversal densities (open circles) are seen to be lower than the current inversion densities by several factors.

### 3.2. Solving SC equations in dielectrically inhomogeneous systems

In the previous paragraphs, we have considered the consequences of the charge reversal effect in different settings. In the next section, we will focus on the image-charge effects in dielectrically inhomogeneous systems.

*3.2.1. Inversion scheme for the solution of the SC equations.* In this section we present the solution of the SC equations (10) and (11) in dielectrically inhomogeneous systems. The technical details of the solution scheme that can be found in [6, 7] will be briefly explained for the case of neutral interfaces. In this case, where the average potential $\psi(\mathbf{r})$ is zero, the fluctuation-enhanced Poisson–Boltzmann equation (10)

vanishes. This leaves us with equation (11) to be solved in order to evaluate the ion density

$$\rho_i(\mathbf{r}) = \rho_b e^{-\frac{q^2}{2}\delta v(\mathbf{r})}, \qquad (48)$$

with the ionic self-energy $\delta v(\mathbf{r})$ defined by equation (12). The iterative solution strategy consists of recasting the differential equation (11) in the form of an integral equation. To this end, we re-express equation (14) as

$$[\nabla^2 - \kappa_b^2 e^{-V_w(\mathbf{r})}]v(\mathbf{r}, \mathbf{r}') = -4\pi\ell_B\delta(\mathbf{r} - \mathbf{r}')$$
$$= -4\pi\ell_B\delta n(\mathbf{r})v(\mathbf{r}, \mathbf{r}') \qquad (49)$$

where we defined the number-density correction function

$$\delta n(\mathbf{r}) = 2q^2\rho_b e^{-V_w(\mathbf{r})}\left[1 - e^{-\frac{q^2}{2}\delta v(\mathbf{r})}\right]. \qquad (50)$$

Introducing now the DH-kernel

$$v_0^{-1}(\mathbf{r}, \mathbf{r}') = -\frac{1}{4\pi\ell_B}\{\nabla^2 - \kappa_b^2 e^{-V_w(\mathbf{r})}\}\delta(\mathbf{r} - \mathbf{r}') \qquad (51)$$

and using the definition of the Green's function (16), one can invert equation (49) and finally obtain

$$v(\mathbf{r}, \mathbf{r}') = v_0(\mathbf{r}, \mathbf{r}') + \int d\mathbf{r}'' v_0(\mathbf{r}, \mathbf{r}'')\delta n(\mathbf{r}'')v(\mathbf{r}'', \mathbf{r}'). \qquad (52)$$

Equation (52) expresses the solution of the SC-kernel equation (11) as the sum of the Debye–Hückel potential $v_0(\mathbf{r}, \mathbf{r}')$ solution to equation (49) and a correction term associated with the non-uniform charge screening induced by image-charge forces. The iterative solution scheme of equation (52) consists of replacing the potential $v(\mathbf{r}, \mathbf{r}')$ on the rhs with the DH potential $v_0(\mathbf{r}, \mathbf{r}')$ at the first iterative step, inserting the output potential $v(\mathbf{r}, \mathbf{r}')$ into the rhs of the equation at the next iterative level, and continuing this cycle until numerical convergence is achieved. The solution scheme for charged interfaces/nanopores is based on the same inversion idea but technically more involved. The more general scheme can be found in [6, 7].

*3.2.2. Image-charge-induced correlations at planar interfaces.* In figure 7, we display the monovalent ion density profiles obtained from the DH and the SC theories that we compare with MC simulations [6]. The dielectric interface located at $z = 0$ is neutral and the membrane permittivity is $\varepsilon_m = 1$. We emphasize that this configuration is also relevant to the water–air interface, whose surface tension was first calculated by Onsager and Samaras [28]. Because their calculation was based on the uniform screening approximation corresponding in our case to the DH approach, the latter is called the Onsager approximation as well. The separation distance is rescaled by the ion size $a_i$, introduced in order to stabilize the MC simulations. At the salt density $\rho_b = 0.01$ M (top plot), the SC result exhibits a very good agreement with the MC simulations while the DH-theory slightly deviates from the MC data, although the error is minor. At this bulk salt concentration where the electrostatic coupling parameter $\Gamma = \kappa_b\ell_B \approx 0.2$ corresponds to the weak-coupling regime, the accuracy of the DH-theory is expected. At the much higher salt density $\rho_b = 0.2$ M (bottom plot), the SC-theory exhibits
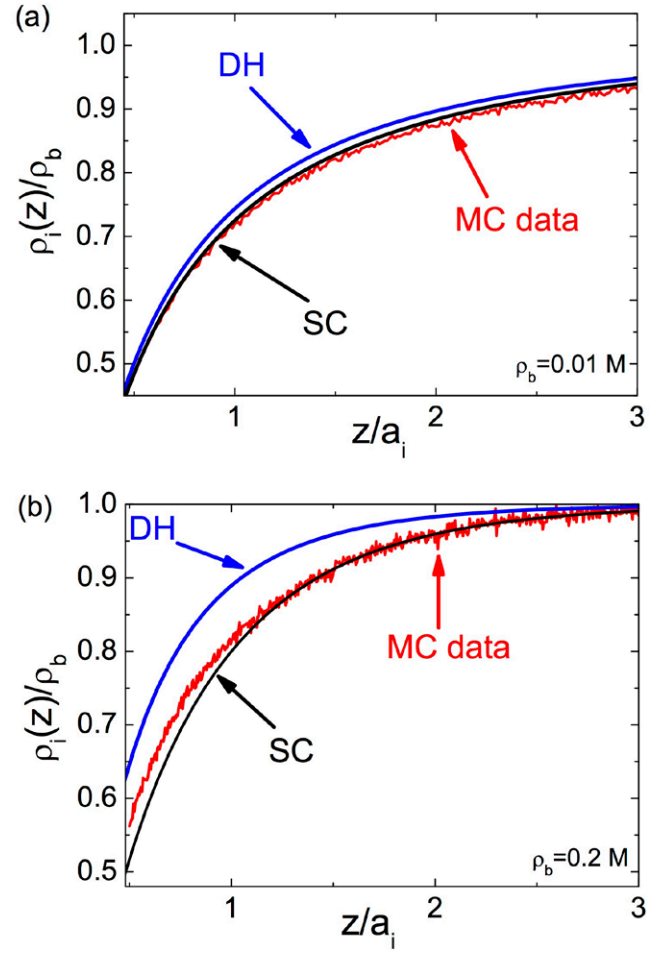


**Figure 7.** Ion density profiles at the dielectric interface against the distance from the surface with $\varepsilon_m = 1$, $\varepsilon_w = 80$, and ion diameter $a_i = 4.25$ Å at the bulk ion concentration (a) $\rho_b = 0.01$ M and (b) $\rho_b = 0.2$ M. The red lines are MC simulation data, the blue lines the DH theory, and the black lines are from the SC scheme (52). The theoretical curves and MC data are from [6].

a good agreement with the MC data but the DH-result overestimates the ion density over the whole interfacial regime.

The inaccuracy of the DH-result is due to the fact that the ion density $\rho_b = 0.2$ M corresponds to the intermediate coupling regime $\Gamma \approx 1$. The overestimation of the ion density stems from the non-uniform salt screening of the image-charge potential at the interface. The mobile ions that screen this potential also being subject to image-charge forces, the interfacial charge screening is lower than the bulk screening. As the DH-theory assumes a constant screening parameter $\kappa_b$, it cannot account for the reduced screening at the interface. In the SC-theory, this effect is taken into account by the second term on the rhs of equation (52), correcting the uniform screening approximation of the DH-theory. We also note that in the close vicinity of the interface, the SC-theory slightly deviates from the MC result. This may be due to ionic hard-core effects neglected so far in the SC-formalism. The weak deviation of the SC theory from the MC data is likely to result from excluded volume effects related to ion size but absent in the SC theory. Although the inclusion of ion size is still an open issue, the excluded volume effects can be included into the present SC theory via repulsive Yukawa interactions (see e.g. [24]).

*3.2.3. Image-charge effects on ion transport through α-Hemolysin pores.* The most significant implication of image-charge correlations is found in electrophoretic charge transport through strongly confined α-hemolysin pores. The particularly low conductivity of these pores cannot be explained by MF electrophoresis. As in the previous section, we will model the pore as a neutral cylinder with a radius of $d = 8.5$ Å and a length of $L = 10$ nm [26] (see figure 3). In the most general case, the pore may be blocked by a single-stranded DNA molecule with a radius of $a = 5.0$ Å [26]. The pore also contains the monovalent electrolyte solution KCl. Under an external potential gradient $\Delta V$, the total velocity of the positive or negative ionic species $u_\pm (r) = u_c (r) + u_{T\pm} (r)$ is composed of the convective velocity $u_c(r)$ given by equation (44), and the drift velocity

$$u_{T\pm} (r) = \pm \mu_\pm \frac{\Delta V}{L}, \tag{53}$$

where $\mu_\pm$ stands for the ionic mobility. The ionic current is given by

$$I = 2\pi e \sum_{i=\pm} q_i \int_a^d \mathrm{d}r r \rho_i(r) u_i(r). \tag{54}$$

Inserting the total velocity $u(r)$ and the ion number density $\rho_i(r)$ into equation (54), the conductivity takes the form of a linear response relation $I = G\Delta V$, where $G$ stands for pore conductance (see [10] for its functional form).

In figure 8(a), we illustrate the conductance of a DNA-free α-hemolysin pore against the reservoir salt density. It is seen that the classical bulk conductivity $G = \pi e \rho_{\mathrm{ib}}(\mu_+ + \mu_-)d^2/L$ overestimates the experimental conductance data by an order of magnitude. However, the SC-theory that can account for image-charge interactions lowers the MF-theory to the order of magnitude of experimental data, with a quantitative agreement at low ion densities and a qualitative agreement at high concentrations. The weak pore conductivity is induced by image-charge interactions between the low permittivity membrane and the nanopore. The radius of these pores being comparable with the Bjerrum length $d \approx \ell_B$, this results in strongly repulsive polarization forces excluding ions from the pore medium and reducing the net conductance.

Figure 8(b) displays the conductance of the same α-hemolysin pore blocked now by the single-stranded DNA (see caption for the characteristic parameters of the DNA molecule). One notes that unlike the conductance of DNA-free pores exhibiting a linear increase with the salt density, the blocked pore conductance rises non-linearly at high densities but weakly changes with salt at dilute concentrations. As the PB-conductivity increases linearly with salt density (dashed red curve), the non-linear behaviour of the blocked pore conductivity is clearly a non-MF effect. One also notes that the SC theory can reproduce the non-linear shape of the experimental conductivity data accurately.

In [10], it is shown that the low density conductance of the blocked pore is given by

$$G = \frac{2\pi e}{L} \mu_+ \sigma_p a. \tag{55}$$

The limiting law (55) is displayed in figure 8(b) by the dashed horizontal curve. This law is independent of the salt
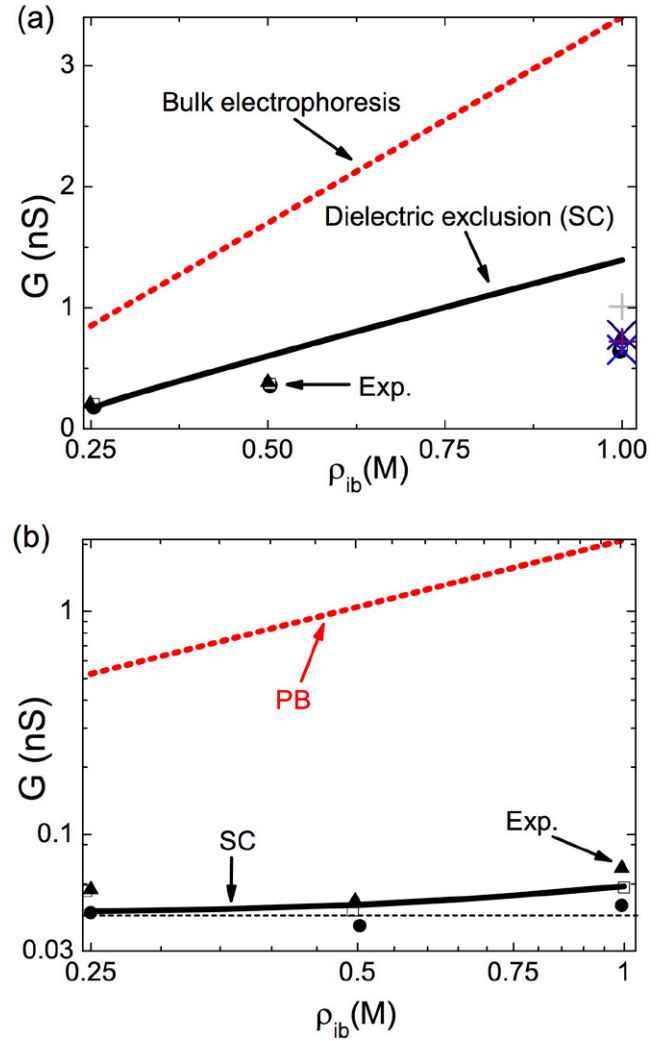


**Figure 8.** (a) Conductivity of an α-hemolysin pore against the reservoir concentration of the KCl solution. The pore, modelled as an overall neutral cylinder ($\sigma_m = 0.0$ C m$^{-2}$), has a radius of $d = 8.5$ Å and a length of $L = 10$ nm. Experimental data: black circles, triangles, and open squares from figure 2 of [26], and the additional data at the bulk ion density $\rho_{\mathrm{ib}} = 1.0$ M from [29] (plus symbol) and table 1 of [30] (cross symbols). (b) The pore in (a) is blocked by a single-stranded DNA molecule with a radius of $a = 5.0$ Å [26] and a dielectric permittivity of $\varepsilon_p = 50$. The effective smeared charge distribution of the ss-DNA is fixed to a value $\sigma_p = 0.012$ e nm$^{-2}$ providing the best fit with the experimental data (symbols) taken from figure 3 of [26].

concentration and depends only on the mobility of counter-ions. Indeed, this counter-ion-driven charge conductivity results from the competition between repulsive image-charge interactions and attractive DNA-counter-ion interactions driven by the pore's electro-neutrality. More precisely, as one lowers the bulk ion density, image-charge forces strongly excluding the ions cannot lead to a total ionic rejection, since a minimum number of ions should stay inside the pore in order to screen the DNA charge. In the dilute concentration regime of figure 8(b), these counter-ions contribute solely to the pore conductance. Hence, the low density limit of pore conductance corresponds to a non-MF counter-ion regime, whose density is fixed by the DNA surface charge rather than

the bulk ion density. At high bulk ion densities, the chemical equilibrium between the pore and bulk media takes over. As a result, co-ions penetrate into the pore and the conductance starts rising with the bulk salt density.

This discussion concludes section 3 of the review, covering the solutions of the self-consistent equations for systems with continuum dielectric properties. In the subsequent section, we turn to the effects of charge correlations in solvent-explicit electrolyte models.

## 4. The dipolar Poisson–Boltzmann equation

In the previous section we have developed a theoretical treatment of current soft matter problems in which the solvent structure is modelled sufficiently well by the assumption of continuous dielectric media—in particular of the solvent—and hence can be described in terms of a dielectric constant. This description is one of scale: if one has to consider systems on molecular scales, this assumption becomes questionable. There has, therefore, been recent interest in including solvent properties more explicitly with the Poisson–Boltzmann theory, and one such example is the family of models which include, as a first step, solvent properties in the form of molecular dipoles. This is done first within the point dipole limit, which allows the formulation local to be kept local. The properties of these theories within mean-field treatments and their application to protein electrostatics have been discussed in a series of papers in recent years [12, 13, 31–38], see also the review [39].

### 4.1. Self-consistent equations for point-dipoles and ions

Here, we derive the variational equations for ions in a point-dipole solvent. The liquid is assumed to be in contact with charged slit membrane walls, though the formulation is valid in all geometries. The solvent geometry and the fluid configuration is shown for slit membranes in figure 7. As the self-consistent equations derived here are novel, we present the derivation in detail.

The grand canonical partition function of ions and dipolar solvent molecules in contact with fixed charge distributions is given by the functional integral over potential configurations $\mathcal{Z}_G = \int \mathcal{D}\phi \, e^{-H[\phi]}$ [12, 13], with the Hamiltonian

$$H[\phi] = \int d\mathbf{r} \left[ \frac{[\nabla\phi(\mathbf{r})]^2}{8\pi\ell_B(r)} - i\sigma(\mathbf{r})\phi(\mathbf{r}) \right] - \int \frac{d\mathbf{r}\, d\mathbf{\Omega}}{4\pi} \Lambda_s \, e^{-V_s(\mathbf{r})+i\mathbf{p}\cdot\nabla\phi}$$
$$- \sum_i \Lambda_i \int d\mathbf{r} \, e^{-V_i(\mathbf{r})+iq_i\phi(\mathbf{r})} \tag{56}$$

where we introduced the dipole moment $\mathbf{p} = -Q\mathbf{a}$, and dipolar and ionic wall potentials $V_s(\mathbf{r})$ and $V_i(\mathbf{r})$. In equation (56), the first integral term accounts for the electrostatic energy of freely propagating waves in a vacuum. It is important to note that the Bjerrum length in a vacuum $\ell_B = e^2/(4\pi\varepsilon_0 k_B T)$ differs from the one used in the previous chapter for the dielectric continuum model: the dielectric constant of water is absent, as the dipoles explicitly model water properties. The second term of equation (56) is the contribution from solvent molecules

modelled as point dipoles with fugacity $\Lambda_s$. Finally, the third term is due to the mobile ions with fugacity $\Lambda_i$. As stated in the introduction, the SC equations can be derived from a variational extremization principle. The grand potential to be minimized has the form [3]

$$\Omega_v = \Omega_0 + \langle H - H_0 \rangle_0, \tag{57}$$

where the bracket $\langle \cdot \rangle_0$ denotes the field-theoretic average with respect to the quadratic reference Hamiltonian of the form of equation (2),

$$H_0 = \frac{1}{2} \int_{\mathbf{r},\mathbf{r}'} [\phi(\mathbf{r}) - \psi(\mathbf{r})]v^{-1}(\mathbf{r},\mathbf{r}')[\phi(\mathbf{r}') - \psi(\mathbf{r}')]. \tag{58}$$

In equation (58), we introduced the trial external potential $\psi(\mathbf{r})$ and the electrostatic kernel $v^{-1}(\mathbf{r},\mathbf{r}')$. First, we note that in equation (57), the part of the grand potential corresponding to the Gaussian fluctuations of the electrostatic potential is given by $\Omega_0 = -\text{Tr}\ln[v]/2$. Evaluating the field-theoretic averages in equation (57), one obtains the variational grand potential in the form of the following fairly involved expression

$$\Omega_v = -\frac{1}{2}\text{Tr}\ln[v] + \int \frac{d\mathbf{r}}{8\pi\ell_B}[\nabla\psi(\mathbf{r})]^2 - i\int d\mathbf{r}\sigma(\mathbf{r})\psi(\mathbf{r})$$
$$+ \int \frac{d\mathbf{r}\, d\mathbf{r}'}{8\pi\ell_B} \delta(\mathbf{r}-\mathbf{r}')\nabla_{\mathbf{r}} \cdot \nabla_{\mathbf{r}'}v(\mathbf{r},\mathbf{r}')$$
$$- \sum_i \Lambda_i \int d\mathbf{r} \, e^{-V_i(\mathbf{r})+iq_i\psi(\mathbf{r})-\frac{q_i^2}{2}\int d\mathbf{r}'\delta(\mathbf{r}-\mathbf{r}')v(\mathbf{r},\mathbf{r}')}$$
$$- \Lambda_s \int d\mathbf{r}\frac{d\mathbf{\Omega}}{4\pi} \, e^{-V_s(\mathbf{r})+i\mathbf{p}\cdot\nabla_{\mathbf{r}}\psi(\mathbf{r})-\frac{1}{2}\int d\mathbf{r}'\delta(\mathbf{r}-\mathbf{r}')(\mathbf{p}\cdot\nabla_{\mathbf{r}})(\mathbf{p}\cdot\nabla_{\mathbf{r}'})v(\mathbf{r},\mathbf{r}')}. \tag{59}$$

The ionic and solvent number densities follow from the thermodynamic relations $\rho_i(\mathbf{r}) = \delta\Omega_v/\delta V_i(\mathbf{r})$ and $\rho_s(\mathbf{r}) = \delta\Omega_v/\delta V_s(\mathbf{r})$. One finds

$$\rho_i(\mathbf{r}) = \Lambda_i \, e^{-V_i(\mathbf{r})-q_i\psi(\mathbf{r})-\frac{q_i^2}{2}v(\mathbf{r},\mathbf{r})} \tag{60}$$

$$\rho_s(\mathbf{r}) = \Lambda_s \int \frac{d\mathbf{\Omega}}{4\pi} \, e^{-V_s(\mathbf{r})+i\mathbf{p}\cdot\nabla_{\mathbf{r}}\psi(\mathbf{r})-\frac{1}{2}\int d\mathbf{r}'\delta(\mathbf{r}-\mathbf{r}')(\mathbf{p}\cdot\nabla_{\mathbf{r}})(\mathbf{p}\cdot\nabla_{\mathbf{r}'})v(\mathbf{r},\mathbf{r}')}. \tag{61}$$

In the bulk region, where the electrostatic potential vanishes, $\psi(\mathbf{r}) \to 0$, and the propagator satisfies spherical symmetry, $v(\mathbf{r},\mathbf{r}') \to v^b(\mathbf{r} - \mathbf{r}')$, from equations (60) and (61) one gets the relation between the bulk densities and fugacities as

$$\rho_{ib} = \Lambda_i \, e^{-\frac{q_i^2}{2}v^b(\mathbf{r}-\mathbf{r})} \tag{62}$$

$$\rho_{sb} = \Lambda_s \, e^{-\frac{1}{2}\int d\mathbf{r}'\delta(\mathbf{r}-\mathbf{r}')(\mathbf{p}\cdot\nabla_{\mathbf{r}})(\mathbf{p}\cdot\nabla_{\mathbf{r}'})v^b(\mathbf{r}-\mathbf{r}')}. \tag{63}$$

Passing from equations (60)–(63), we accounted for the fact that in the bulk region, the dipolar potential of mean force (PMF) in the exponential is independent of the dipolar orientation.

The SC equations follow from the optimization of the variational grand potential with respect to the electrostatic potential $\psi(\mathbf{r})$ and propagator $v(\mathbf{r},\mathbf{r}')$, i.e. $\delta\Omega_v/\delta\psi(\mathbf{r}) = 0$ and $\delta\Omega_v/\delta v(\mathbf{r},\mathbf{r}') = 0$. By evaluating the functional derivatives and setting them to zero, replacing the solvent and ion fugacities

by the bulk densities according to equations (62) and (63), and passing to the real electrostatic potential via the transformation $\psi(\mathbf{r}) \to i\psi(\mathbf{r})$, after lengthy algebra one gets the variational equations in the form

$$\nabla \cdot [\nabla \psi(\mathbf{r}) + 4\pi \ell_B \mathbf{P}(\mathbf{r})] + 4\pi \ell_B \sum_i q_i \rho_i(\mathbf{r}) = -4\pi \ell_B \sigma(\mathbf{r})$$

$$(64)$$

$$\partial_\mu \varepsilon^{\mu\nu}(\mathbf{r}) \partial_\nu v(\mathbf{r}, \mathbf{r}') - 4\pi \ell_B \sum_i q_i^2 \rho_i(\mathbf{r}) v(\mathbf{r}, \mathbf{r}') = -4\pi \ell_B \delta(\mathbf{r} - \mathbf{r}'),$$

$$(65)$$

where we introduced the polarization field

$$\mathbf{P}(\mathbf{r}) = -\rho_{sb} \int \frac{d\Omega}{4\pi} \mathbf{p} \, e^{-\varphi_d(\mathbf{r}, \Omega)} \qquad (66)$$

that corresponds to the average dipolar polarization, the ion number density

$$\rho_i(\mathbf{r}) = \rho_{ib} \, e^{-V_i(\mathbf{r}) - q_i \psi(\mathbf{r}) - \frac{q_i^2}{2} \delta v(\mathbf{r})} \qquad (67)$$

with the renormalized equal-point propagator

$$\delta v(\mathbf{r}) = \lim_{\mathbf{r}' \to \mathbf{r}} [v(\mathbf{r}, \mathbf{r}') - v^b(\mathbf{r} - \mathbf{r}')], \qquad (68)$$

and the dielectric permittivity tensor

$$\varepsilon_{\mu\nu}(\mathbf{r}) = \delta_{\mu\nu} + 4\pi \ell_B \rho_{sb} \int \frac{d\Omega}{4\pi} p_\mu p_\nu \, e^{-\varphi_d(\mathbf{r}, \Omega)} \qquad (69)$$

corresponding to the fluctuations of the dipole moment. In equations (66) and (69), we also introduced the dipolar PMF

$$\varphi_d(\mathbf{r}, \Omega) = V_s(\mathbf{r}) + \mathbf{p} \cdot \nabla \psi(\mathbf{r}) + \varphi_v(\mathbf{r}, \Omega) \qquad (70)$$

with the short-hand notation for the part of the dipolar PMF involving the Green's function

$$\varphi_v(\mathbf{r}, \Omega) = \frac{1}{2} \lim_{\mathbf{r}' \to \mathbf{r}} (\mathbf{p} \cdot \nabla_\mathbf{r})(\mathbf{p} \cdot \nabla_{\mathbf{r}'})[v(\mathbf{r}, \mathbf{r}') - v^b(\mathbf{r} - \mathbf{r}')].$$

$$(71)$$

### 4.2. Differential capacitance of low dielectric materials

The variational equations for the dipolar PB theory having been established, we now discuss the effect of the interfacial solvent configuration on the differential capacitance of low dielectric materials such as carbon based substrates of permittivity $\varepsilon_m \approx 1$ [40]. We consider a dipolar liquid with the bulk density $\rho_{db} = 50.8$ M and the molecular dipole moment $p_0 = 1$ Å, which corresponds to the bulk dielectric permittivity $\varepsilon_w = 71$. The liquid containing a monovalent symmetric electrolyte ($q_+ = -q_- = 1$) is in contact with a charged dielectric membrane surface located at $z = 0$ and separating the dipolar fluid from a membrane with permittivity $\varepsilon_m$. This configuration corresponds to the infinite separation distance limit $d \to \infty$ of the planar geometry of figure 9. The results obtained in [40] within a restricted variational ansatz can be rederived from the dipolar SC theory introduced in the previous section. This consists of solving the dipolar equations derived in the previous section by approximating the solution of the kernel equation (65) with the solution of the DH-equation

$$\nabla^2 v(\mathbf{r}, \mathbf{r}') - \kappa_b^2 e^{-V_w(\mathbf{r}) - \frac{q_i^2}{2} \delta v(z)} v(\mathbf{r}, \mathbf{r}') = -4\pi \ell_B \delta(\mathbf{r} - \mathbf{r}') \quad (72)$$

in planar geometry. For the simple dielectric interface with the liquid located at $z > 0$, the solution reads as [22]

$$v(\mathbf{r}, \mathbf{r}') = \frac{\ell_B}{\varepsilon_w} \int \frac{d^2\mathbf{k}}{2\pi p_b} e^{i\mathbf{k} \cdot (\mathbf{r}_\| - \mathbf{r}'_\|)} [e^{-p|z-z'|} + \Delta_b e^{-p(z+z')}] \quad (73)$$

with the bulk dielectric discontinuity parameter $\Delta_b = (\varepsilon_w p_b - \varepsilon_m k)/(\varepsilon_w p_b + \varepsilon_m k)$. Evaluating equations (67) and (68) with the continuum Green's function (73), one gets the fluctuation-enhanced dipolar PB (EDPB) equation (64) in the form

$$\frac{\partial}{\partial z} \tilde{\varepsilon}(z) \frac{\partial \psi(z)}{\partial z} + 4\pi \ell_B \sigma(z) + 4\pi \ell_B \sum \rho_i(z) q_i = 0, \quad (74)$$

where we defined the ion number density

$$\rho_i(z) = \rho_{b,i} \theta(z) e^{-q_i \psi(z) - V_c(z)} \qquad (75)$$

with the Heaviside theta function $\theta(z)$, and the local dielectric permittivity function

$$\tilde{\varepsilon}(z) = 1 + \frac{4\pi}{3} \ell_B p_0^2 \rho_{sb} \theta(z) e^{-U_d(z)} J(z), \qquad (76)$$

with the ionic and dipolar potentials

$$V_c(z) = \frac{q^2 \ell_B}{2 e_w} \int_0^\infty \frac{dk k}{\rho_b} \Delta e^{-2\rho_b z}, \qquad (77)$$

$$U_d(z) = \frac{\ell_B p_0^2}{4 e_w} \int \frac{dk k^3}{\rho_b} \Delta e^{-2\rho_b z} \qquad (78)$$

$$T_d(z) = \frac{\ell_B p_0^2}{4 e_w} \int \frac{dk k}{\rho_c} (2\rho_b^2 - k^2) \Delta e^{-2\rho_b z}, \qquad (79)$$

and the auxiliary functions

$$J(z) = \frac{3\sqrt{\pi}}{8 T_d^{3/2}(z)} e^{\frac{p_0^2 \psi'^2(z)}{4 T_d(z)}} \{ \text{Erf}[\Psi_+(z)] + \text{Erf}[\Psi_-(z)] \}$$
$$- \frac{3 e^{-T_d(z)}}{2 T_d(z)} \frac{\sinh[p_0 \psi'(z)]}{p_0 \psi'(z)} \qquad (80)$$

$$\Psi_\pm(z) = \frac{2 T_d(z) \pm p_0 \psi'(z)}{2 \sqrt{T_d(z)}}. \qquad (81)$$

We note that the dielectric permittivity function (76) differs from the permittivity tensor (69) since the former is related to the average dipole moment (69) as $\varepsilon(z) = 1 + 4\pi \ell_B P_z(z)/\psi'(z)$ rather than to dipole moment fluctuations. We also emphasize that in the bulk region, the permittivity tends to the bulk Debye–Langevin form, i.e. $\varepsilon(z \to \infty) = \varepsilon_w = 1 + 4\pi \ell_B p_0^2 \rho_{sb}/3$.

The vanishing potential limit of the double layer differential capacitance is given by

$$C_d = \lim_{\sigma_s \to 0} \frac{q e^2}{k_B T} \left| \frac{\partial \sigma_s}{\partial \psi(0)} \right|. \qquad (82)$$

In figure 10 we plot the capacitance (82) from different theories. The open black squares display the experimental data
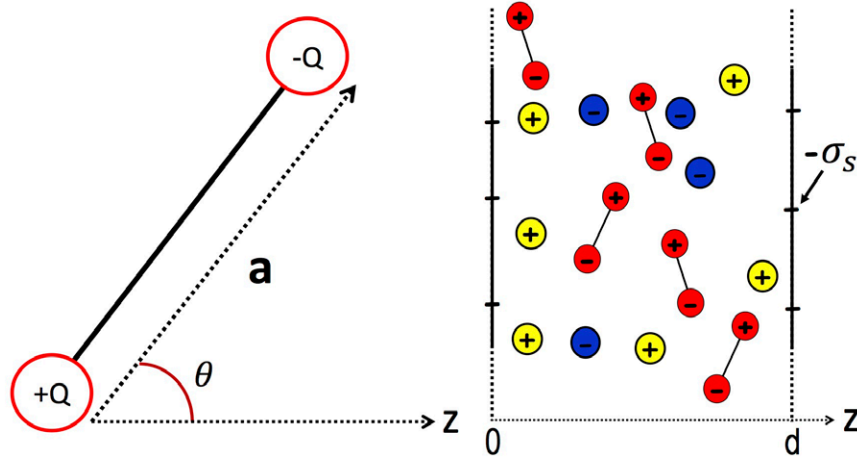
**Figure 9.** Left: charge geometry of solvent molecules of size $a = 1$ Å; the charges of valency $Q = 1$ are placed at the ends. Right: geometry of the slit nanopore with a surface charge of $-\sigma_s \leqslant 0$ confining the solvent molecules (red dipoles), anions (blue circles), and cations (yellow circles).

obtained for various types of monovalent electrolytes at different densities (see [41] for details). One sees that both the Gouy–Chapman capacitance (PB) $C_{GC} = (\varepsilon_w \kappa_b)^{-1}$ and the MF level dipolar PB equation [12, 13] overestimate the experimental data by an order of magnitude. The solvent-implicit modified-PB (MBP) equation [22], considering exclusively the ion-image interactions, slightly lowers the theoretical curve—although the disagreement with the experimental data is still very strong. However, the prediction of the EDPB equation (74) corrects the PB and DPB results by an order of magnitude and exhibits a good quantitative agreement with the experimental data.

We further analyze the strong variations of the predictions from one theory to the other and to probe the underlying mechanism behind the low capacitance of carbon substrates. Noting that the capacitance (82) is directly related to the electrostatic potential, we plotted the latter in figure 11(a). In figure 11(b), we also show the reduced dielectric permittivity profile from equation (76) and the non-dimensional screening function $\kappa^2(z)/\kappa_b^2 = e^{-V_c(z)}$. It is seen that the potential profile is composed of three regions (see also inset). In the vicinity of the charged surface, the potential exhibits a linear drop towards the interface. This strong decrease results from the interfacial dielectric screening deficiency illustrated in figure 11(b) by the local permittivity curve. The dielectric permittivity reduction is induced in turn by the interfacial solvent depletion driven by solvent-image interactions and amplifies the PB surface potential by a factor of five. This first layer in the potential profile is followed by a second region where the potential rises linearly but with a lower slope. The linear behaviour of the potential is now due to the charge screening deficiency resulting from the image-charge interactions $V_c(z)$ of equation (77) (see the screening function curve in figure 11(b)). Finally, at large separation distances from the interface $z \gtrsim 5$ Å, the potential decays exponentially fast. This region corresponds to the diffuse layer governed by charge screening. The latter is the only effect taken into account by the PB-equation.
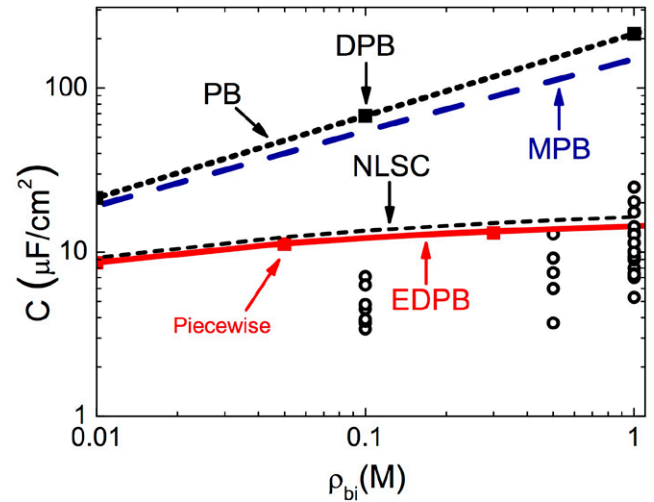


**Figure 10.** Differential capacitance against the bulk ion concentration for $\sigma_s \to 0$, $\varepsilon_m = 1$, and $\varepsilon_w = 71$. The black circles are the experimental data, the red solid curve is the result of the EDPB equation (74), the red squares are from equation (84), the dashed blue line is the MPB result, the dotted black line is the GC capacitance, and the black squares correspond to the prediction of the DPB equation. The open circles are the experimental capacitance data from [41].

In order to have a deeper analytical insight into the behaviour of the capacitance data in figure 10, one can derive an analytical capacitance formula. To this end, we will develop a restricted variational approach. Based on the piecewise shape of the electrostatic potential in figure 11(b), we assume that the potential $\psi(z)$ is the solution of equation (74) with a piecewise permittivity profile $\varepsilon(z) = \theta(h_s - z) + \varepsilon_w \theta(z - h_s)$ and screening parameter $\kappa(z) = \kappa_c \theta(z - h_c)$. In these functions, the trial parameters $h_c$ and $h_s$, corresponding respectively to the charge and solvent depletion lengths, will be determined from a numerical extremization of the grand potential (57). Accounting for the continuity of the potential $\psi(z)$ and the displacement field $\varepsilon(z)\psi'(z)$ at $z = 0$, $z = h_s$, and $z = h_c$, the piecewise potential profile takes the form
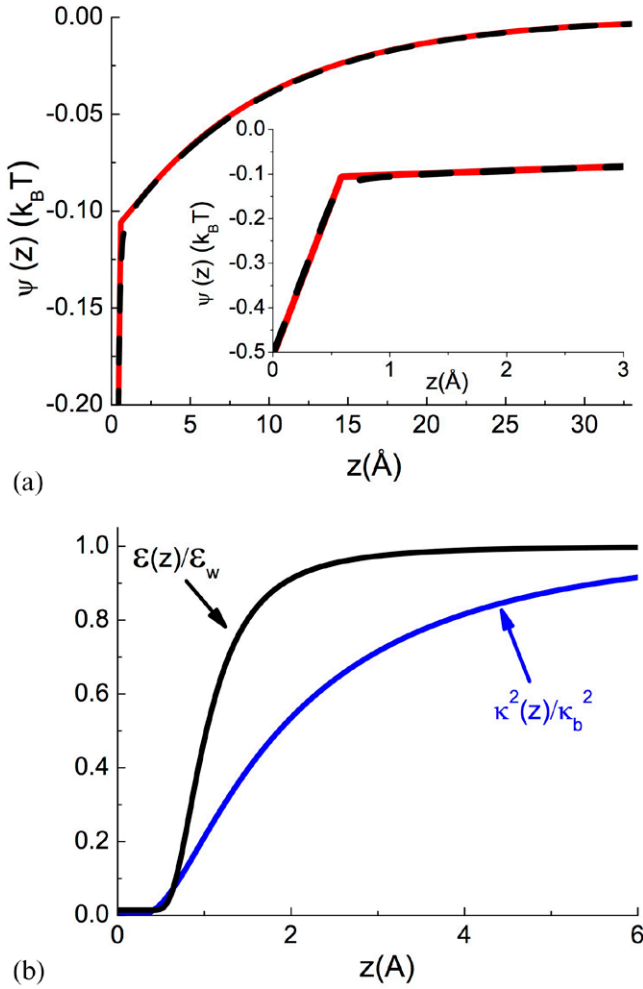
**Figure 11.** (a) Electrostatic potential profile ($\sigma_s = 0.01\,\text{nm}^{-2}$) and (b) renormalized density and dielectric permittivity profiles for $\varepsilon_w = 71$ and $\rho_{bi} = 0.1\,\text{M}$. The red line in (a) is from the restricted variational ansatz equation (83) and the dashed black line corresponds to the solution of the EDPB equation.

$$\psi(0 < z \leqslant h_s) = -\frac{2}{\mu\kappa_b}[1 + \kappa_b(h_c - h_s)] + \frac{2\varepsilon_w}{\mu}(z - h_s)$$

$$\psi(h_s \leqslant z \leqslant h_c) = -\frac{2}{\mu\kappa_b} + \frac{2}{\mu}(z - h_c)$$

$$\psi(z \geqslant h_c) = -\frac{2}{\mu\kappa_b}e^{-\kappa_b(z - h_c)}. \tag{83}$$

The trial lengths are determined by inserting the piecewise potential (83) into the grand potential (57) and optimizing the latter with respect to the parameters $h_s$ and $h_c$. The result of the optimization at bulk ion density $\rho_{ib} = 0.1\,\text{M}$ and surface charge $\sigma_s = 0.01\,\text{nm}^{-2}$ is shown in figure 11(a) by the dashed curve. The comparison with the exact numerical solution of equation (74) shows that the agreement is very good. Evaluating the differential capacitance according to equation (82) with the piecewise potential (83), one finds

$$C_d = \frac{\varepsilon_w\kappa_b}{1 + \kappa_b(h_c - h_s) + \varepsilon_w\kappa_b h_s}. \tag{84}$$

The prediction of this analytical formula reported in figure 10 (red squares) shows that the formula reproduces the prediction of the EDPB equation very accurately. Now, we note that the inverse capacitance is composed of three terms, $C_d^{-1} = C_{\text{GC}}^{-1} + C_c^{-1} + C_s^{-1}$. The first contribution of the Gouy–Chapman capacitance corresponding to the diffuse layer was introduced above. The second contribution $C_c^{-1} = (h_c - h_s)\varepsilon_w$, associated with the ionic depletion layer, brings the correction that lowers the capacitance curve to the MPB result in figure 10. Finally, the third term $C_s^{-1} = h_s$, due to the solvent depletion responsible for the interfacial dielectric screening deficiency, makes the most important contribution to the differential capacitance by lowering the latter to the order of magnitude of the experimental data. Thus, the particularly weak capacitance of low permittivity carbon-based materials is driven by their hydrophobicity.

In the next chapter, we relax the present point-dipole approximation and consider the non-local electrostatic interactions associated with the extended charge structure of solvent molecules.

## 5. Non-locality in the dipolar Poisson–Boltzmann equation

The notion of non-local electrostatics already has a long history in soft matter. On sufficiently small scales, the dielectric response of a medium becomes wave-vector dependent, see [42–44] and the references therein. In many descriptions in the literature, this behaviour has been modelled in a phenomenological fashion by invoking simplified dielectric functions. The relevance of this effect has also been shown in recent MD simulations [45, 46]. The advantage of our present description of a 'structured' solvent is that we can include non-local effects in a direct and natural way, just by relaxing the condition of point dipoles in the DPB-model [14]; this will be the topic of the last section of this topical review.

### 5.1. Non-local self-consistent equations

In this section, we discuss the dipolar liquid model introduced in [14] and the associated non-local self-consistent (NLSC) equations derived in [15]. Thus, we relax the point-dipole approximation and model the solvent molecules as dipoles with finite molecular size $a$ (see figure 9). The liquid enclosed in a slit pore of size $d$ also includes $p$ ionic species, and each species $i$ with valency $q_i$. The grand-canonical partition function of this liquid is given by the functional integral $Z_G = \int \mathcal{D}\phi\, e^{-H[\phi]}$, with the Hamiltonian functional

$$H[\phi] = \frac{k_{\text{B}}T}{2e^2}\int d\mathbf{r}\, \varepsilon_0(\mathbf{r})[\nabla\phi(\mathbf{r})]^2 - i\int d\mathbf{r}\sigma(\mathbf{r})\phi(\mathbf{r})$$
$$- \Lambda_s\int\frac{d\mathbf{r}\,d\mathbf{\Omega}}{4\pi}e^{-V_s(\mathbf{r},\mathbf{a})}e^{iQ[\phi(\mathbf{r}) - \phi(\mathbf{r}+\mathbf{a})]}$$
$$- \sum_i \Lambda_i\int d\mathbf{r}e^{-V_i(\mathbf{r})}e^{iq\phi(\mathbf{r})}, \tag{85}$$

where $\varepsilon_0(\mathbf{r})$ accounts for the dielectric permittivity contrast between the vacuum and the membrane of permittivities $\varepsilon_0$ and $\varepsilon_m$, respectively. The other parameters have the same definition as in equation (56). We also note that if one takes the point-dipole limit $\mathbf{a} \to 0$ while $p_0 = -Q\mathbf{a}$ remains constant, the dipolar term on the rhs of the functional (85) converges to the dipolar contribution of the point-dipole Hamiltonian (56).

The variational grand potential is obtained along the same lines as for the point-dipole model of section 4. One obtains

$$
\begin{aligned}
\Omega_v = &-\frac{1}{2}\mathrm{Tr}\ln[v] + \int d\mathbf{r}\sigma(\mathbf{r})\psi(\mathbf{r}) \\
&+ \frac{k_B T}{2e^2}\int d\mathbf{r}\varepsilon_0(\mathbf{r})\{\nabla_{\mathbf{r}}\cdot\nabla_{\mathbf{r}'}v(\mathbf{r},\mathbf{r}')|_{\mathbf{r}'\to\mathbf{r}} - [\nabla\psi(\mathbf{r})]^2\} \\
&- \sum_i \Lambda_i \int d\mathbf{r}e^{-V_i(\mathbf{r})}e^{-q_i\psi(\mathbf{r})}e^{-\frac{q_i^2}{2}v(\mathbf{r},\mathbf{r})} \\
&- \Lambda_s \int d\mathbf{r}\frac{d\,\Omega}{4\pi}e^{-V_s(\mathbf{r},\mathbf{a})}e^{-Q[\psi(\mathbf{r})-\psi(\mathbf{r}+\mathbf{a})]}e^{-\frac{Q^2}{2}v_d(\mathbf{r},\mathbf{a})}.
\end{aligned}
\tag{86}
$$

We will now derive the NLSC equations in the plane geometry of figure 9. The general form of these equations can be found in [15]. By evaluating the functional derivatives of the variational grand potential (86) with respect to the trial potentials $v(\mathbf{r},\mathbf{r}')$ and $\psi(\mathbf{r})$, setting the results to zero, and expanding the resulting kernel equation on a Fourier basis according to equation (22), in order to take advantage of the plane symmetry, after long algebra, the NLSC equations take the form

$$
\begin{aligned}
&\frac{k_B T}{e^2}\partial_z\varepsilon_0(z)\partial_z\psi(z) + \sum_i q_i\rho_i(z) + 2Q\rho_{sb}\int_{a_1(z)}^{a_2(z)}\frac{da_z}{2a} \\
&\times \sinh\left[Q\psi(z+a_z) - Q\psi(z)\right]e^{-\frac{Q^2}{2}\delta v_d(z,a_z)} = -\sigma(z)
\end{aligned}
\tag{87}
$$

$$
\begin{aligned}
&-\frac{k_B T}{e^2}[\partial_z\varepsilon_0(z)\partial_z - \varepsilon_0(z)p^2(z)]\tilde{v}_0(z,z') \\
&+ 2Q^2\rho_{sb}\int_{a_1(z)}^{a_2(z)}\frac{da_z}{2a}\cosh[Q\psi(z+a_z)-Q\psi(z)] \\
&\times e^{-\frac{Q^2}{2}\delta v_d(z,a_z)}\{\tilde{v}_0(z,z') - \tilde{v}_0(z+a_z,z')J_0(k|a_\parallel|)\} \\
&= \delta(z-z').
\end{aligned}
\tag{88}
$$

In equations (87) and (88) we defined the ion density

$$
\rho_i(z) = \rho_{ib}e^{-q_i\psi_0(z)}e^{-\frac{q_i^2}{2}\delta v_i(z)-V_i(z)},
\tag{89}
$$

and the ionic and dipolar self-energies

$$
\delta v_i(z) = v(z,z) - v^b(0)
\tag{90}
$$

$$
\delta v_d(z,a_z) = v_d(z,a_z) - 2v^b(0) + 2v^b(a),
\tag{91}
$$

with the bulk limit of the variational kernel $v^b(\mathbf{r}-\mathbf{r}')$, and the auxiliary function $p(z) = \sqrt{k^2 + \kappa_i^2(z)}$ where the local charge screening function is defined as

$$
\kappa_i^2(z) = \frac{e^2}{\varepsilon_0(z)k_B T}\sum_i q_i^2\rho_i(z).
\tag{92}
$$

We also introduced the integral boundaries imposing the impenetrability of the interfaces, $a_1(z) = -\min(a,z)$ and $a_2(z) = \min(a, d-z)$.

The first NLSC equation (87) is the fluctuation-enhanced dipolar PB equation. In this equation, the dipolar charge density corresponding to the integral term is seen to depend on the value of the electrostatic potential at all points in the slit, resulting in the non-locality of this integro-differential equation. This shows that the consideration of the extended solvent structure directly gives rise to the non-locality of the electrostatic interactions. The equation (87) is coupled to the solution of the second NLSC equation (88) for the electrostatic Green's function. In the next part, we discuss the solution of these equations within different approximations.

## 5.2. Solution of NLSC equations at the MF-level and beyond

We will first consider the NLSC equations (87) and (88) at the MF level [15]. In order to take the MF limit, one can evaluate the saddle-point of the Hamiltonian functional (86), i.e. $\delta H[\phi]/\delta\phi(\mathbf{r})|_{\phi=\psi} = 0$, or set in equations (87) and (88) the electrostatic Green's function accounting for charge correlations to zero, $v(\mathbf{r},\mathbf{r}') \to 0$. The non-local PB (NLPB) equation reads as

$$
\begin{aligned}
&\partial_z^2\psi(z) + 4\pi\ell_B\sigma(z) - 8\pi\ell_B\rho_i^b q\sinh[q\psi(z)] \\
&+ 8\pi\ell_B Q\rho_s^b\int_{a_1(z)}^{a_2(z)}\frac{da_z}{2a}\sinh[Q\psi(z+a_z) - Q\psi(z)] = 0,
\end{aligned}
\tag{93}
$$

with the Bjerrum length in air $\ell_B = e^2/(4\pi\varepsilon_0 k_B T) \approx 55$ nm.

We will first investigate equation (93) in the linear response regime of weak surface charges. In order to simplify the presentation, we will also assume that there is a single permeable interface at $z = 0$. In this case, one can set $a_1(z) \to -a$ and $a_2(z) \to a$. Finally, linearizing the terms which are non-linear in the potential $\psi(z)$, the linear NLPB equation follows in the form

$$
\partial_z^2\psi(z) - \kappa_i^2\psi(z) + \kappa_s^2\int_{-a}^{a}\frac{da_z}{2a}[\psi(z+a_z) - \psi(z)] = -4\pi\ell_B\sigma(z)
\tag{94}
$$

with the surface charge distribution $\sigma(z) = -\sigma_s\delta(z)$ and the ionic and solvent screening parameters in the air medium $\kappa_i^2 = 8\pi\ell_B\rho_i^b q_i^2$ and $\kappa_s^2 = 8\pi\ell_B\rho_s^b Q^2$, respectively. One can solve equation (94) on a Fourier basis and obtain

$$
\psi(z) = -8\ell_B\sigma_s\int_0^\infty dk\frac{\cos(kz)}{\kappa_i^2\varepsilon_w + k^2\tilde{\varepsilon}(k)},
\tag{95}
$$

with the Fourier-transformed permittivity

$$
\tilde{\varepsilon}(k) = 1 + 4\pi\ell_B\tilde{\chi}(k)
\tag{96}
$$

and the susceptibility function

$$
\tilde{\chi}(k) = \frac{\kappa_s^2}{4\pi\ell_B k^2}\left[1 - \frac{\sin(ka)}{ka}\right].
\tag{97}
$$

From equation (95), the electric field $E(z) = \psi'(z)$ follows as

$$
E(z) = 8\ell_B\sigma_s\int_0^\infty dk k\frac{\sin(kz)}{\kappa_i^2\varepsilon_w + k^2\tilde{\varepsilon}(k)}.
\tag{98}
$$

We note that equation (98) satisfies the modified Gauss's law $E(z = 0) = 4\pi \ell_\text{B} \sigma_s$, which differs by a factor $\varepsilon_w$ from the usual Gauss's law. In the immediate vicinity of the charged interface where $\kappa_i z \ll 1$, one can neglect the screening term in the denominator of equation (98) and rewrite the electric field as

$$E(z) \simeq \frac{4\pi \ell_\text{B} \sigma_s}{\varepsilon_\text{eff}(z)}, \qquad (99)$$

where we introduced the local effective dielectric permittivity function

$$\varepsilon_\text{eff}(z) = \frac{\pi}{2} \Big/ \int_0^\infty \frac{\text{d}k}{k} \frac{\sin(kz)}{\tilde{\varepsilon}(k)}. \qquad (100)$$

For the leading order in the solvent density $O((\kappa_s a)^2)$, the local permittivity equation (100) takes the simple form

$$\varepsilon_\text{eff}(z) = 1 + \frac{(\kappa_s a)^2}{6} \left\{ 1 - \left( 1 - \frac{z}{a} \right)^3 \theta(a - z) \right\}, \qquad (101)$$

where $\theta(z)$ stands for the Heaviside function. Hence, in the case of pure solvents of low permittivity in contact with weakly charged surfaces, the effective permittivity rises from the air permittivity $\varepsilon_\text{eff}(0) = 1$ to the bulk solvent permittivity $\varepsilon_w = 1 + (\kappa_s a)^2/6$. In figure 12(a), we plotted the non-local permittivity (100) (solid black curve) and its dilute solvent limit (101) (dotted black curve). The model parameters are given in the caption. One notes that the behaviour of the non-local permittivity is characterized by fluctuations around the limiting law (101), with the first two peaks exceeding the bulk permittivity. We emphasize that this structural formation has been previously observed in molecular dynamics simulations with explicit solvents (see e.g. [47]), and also in theoretical models based on integral equations [48]. By a simple consideration of the finite solvent size, the appearance of these oscillations shows that they are induced by the extended solvent charge structure responsible for the non-local dielectric response of the fluid to the membrane charge.

In order to trace the microscopic origin of this structural formation, we consider the solvent charge partition close to the membrane surface. To this end, we will relate the solvent charge density and the effective permittivity in the fluctuation-enhanced limit of the NLSC equation (87). By integrating this equation from the interface at $z = 0$ to any position $z$ in the liquid, and using equation (98), one finds that the dielectric permittivity (100) can be expressed as

$$\frac{1}{\varepsilon_\text{eff}(z)} = 1 - \frac{1}{\sigma_s} \int_0^z \text{d}z' \rho_\text{sc}(z'). \qquad (102)$$

In equation (102), the solvent charge density is

$$\rho_\text{sc}(z) = Q \left[ \rho_{s+}(z) - \rho_{s-}(z) \right], \qquad (103)$$

and the number density of the positive and negative charges making up each solvent molecule is

$$\rho_{s\pm}(z) = \rho_s^b \int_{a_1(z)}^{a_2(z)} \frac{\text{d}a_z}{2a} \text{e}^{-\frac{Q^2}{2}\delta v_d(z, a_z)} \text{e}^{\pm Q[\psi(z + a_z) - \psi(z)]}. \qquad (104)$$

The MF-level solvent density is also given by equation (104) by setting $\delta v_d(z, a_z) = 0$. Equation (102) is essential as it
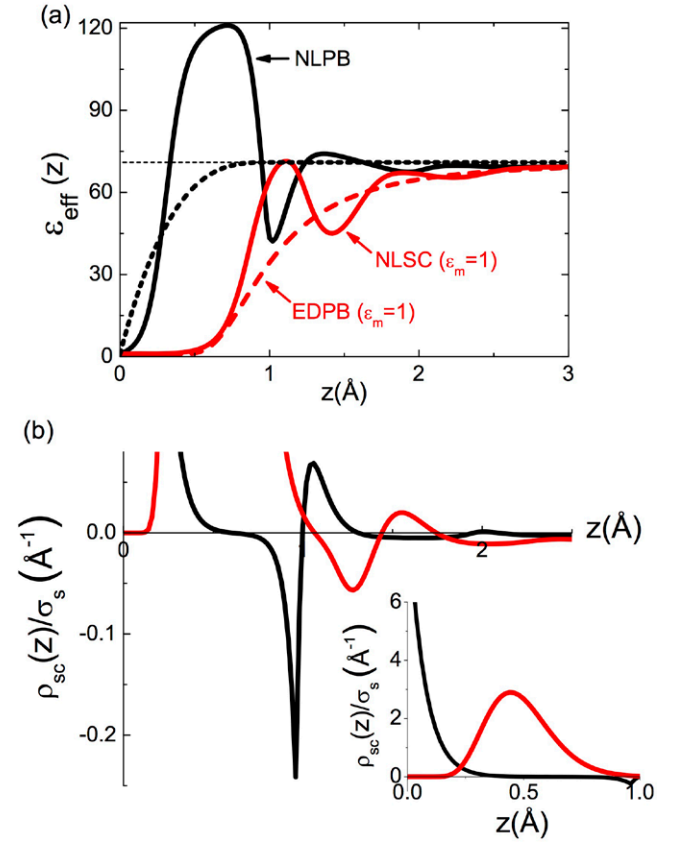


**Figure 12.** (a) Effective dielectric permittivity profile and (b) rescaled polarization charge density obtained from the MF NLPB equation (93) (solid black curves) and the NLSC equation (87) (solid red curves) for the solvent with bulk density $\rho_\text{sb} = 50.8$ M and permittivity $\varepsilon_w = 71$, in contact with a planar interface with surface charge $\sigma_s = 10^{-6}$ e nm$^{-2}$. Salt concentration is $\rho_\text{ib} = 10^{-5}$ M. In (a), the dashed red curve is the permittivity profile of the point-dipole theory (DPB) equation (74). The dotted black curve displays the dilute solvent limit (101) of the NLPB permittivity (100).

indicates that the local value of the dielectric permittivity results from the cumulative solvent charge between the interface and the position $z$ in the liquid. We plotted the MF limit of the solvent charge density (103) in figure 12(b) (black curve). One notes that the solvent response to the charged membrane gives rise to the formation of solvent layers with alternating net charge. More precisely, the immediate vicinity of the interface is characterized by the presence of a positive solvent layer (see the inset) followed by a negative layer (see the main plot) and so on. We also notice that in agreement with equation (102), the boundary between each solvent layer coincides with the maximum or minimum of the dielectric permittivity profile $\varepsilon_\text{eff}(z)$. Thus, the dielectric permittivity fluctuations are induced by the interfacial solvent charge structure.

In order to probe the dielectric discontinuity effects absent in the MF-NLPB equation, we now consider the NLSC equations (87) and (88). Because there is no recipe for the solution of the non-local kernel equation (88), we will approximate its solution by the solution of the DH equation of the local dipolar model. This leaves us with the single non-local equation (87) for the average potential $\psi(z)$ whose numerical solution is also considerably technical. The numerical

relaxation schemes that we have developed can be found in [49] and [50]. In figures 12(a) and (b), we plotted the effective permittivity (102) and the solvent charge density (103) (solid red curves) obtained from the NLSC equation (87) at the membrane permittivity $\varepsilon_m = 1$. In figure 12(b), one sees that the image-dipole effects repelling the solvent molecules from the surface reduce the interfacial solvent charge density. Figure 12(a) shows that this result is an amplification of the surface dielectric void layer, and an overall reduction of the dielectric permittivity of the MF-NLPB theory.

The image-dipole correlations amplify the interfacial dielectric void resulting from the non-local solvent response at the MF-level. We now wish to identify the effect of the extended solvent structure beyond this level. To this end, in figure 12, we compare the dielectric permittivity of the NLSC formalism with the permittivity profile of the point-dipole (EDPB) theory (dashed red curve). One notes that both permittivities are characterized by the same dielectric void layer, with the NLSC permittivity exhibiting fluctuations around the EDP permittivity. This indicates that the strong interfacial dielectric void is driven by solvent-image interactions present both in the local and the non-local formalism. This point is confirmed by figure 10, where we compare the local and non-local capacitance predictions. It is seen that the NLPB capacitance weakly differs from the EDP result. Since we showed that low differential capacitance is induced by surface solvent depletion, the closeness of the local and non-local capacitances is indeed expected. Thus, we can conclude that the non-locality plays no major role in the hydrophobicity of the membrane surface.

## 6. Discussion and conclusions

In this topical review we have presented an introduction to the recently developed variational or self-consistent approach to soft matter electrostatics which allows correlation effects beyond the Poisson–Boltzmann theory to be included. We developed two cases: first, the continuum approach in which the solvent properties are captured by its macroscopic dielectric constant, and second, a model with an explicit solvent in which the solvent properties are modelled with point or finitely sized dipoles. The latter theory is, to our knowledge, the first explicitly formulated example of a 'structured Coulomb fluid' treated beyond mean-field theory, and including non-local effects.

In this work, we have selected a few application examples and developed them in some technical detail with the intention of helping the interested reader in gaining access to the approach. We hope that the illustrative examples we discussed do show the power of the method, which nevertheless comes at a certain computational effort. In many further applications, the equations will in fact only be solvable by numerical methods which are beginning to be developed. The further close confrontation of theoretical results that can be obtained from the self-consistent approach with experimental results and computer simulations on soft matter systems will be crucial for the future development of a systematic approach to correlation effects in soft condensed matter.

## References

[1] Netz R R and Orland H 2000 *Eur. Phys. J. E* **5** 557–74
[2] Naji A, Kanduc M, Forsman J and Podgornik R 2013 *J. Chem. Phys.* **139** 150901
[3] Netz R R and Orland H 2003 *Eur. Phys. J. E* **11** 301–31
[4] Avdeev S M and Martynov G A 1986 *Colloid J. USSR* **48** 535–42
[5] Hatlo M M, Curtis R A and Lue L 2008 *J. Chem. Phys.* **128** 164717
[6] Buyukdagli S, Achim C V and Ala-Nissila T 2012 *J. Chem. Phys.* **137** 104902
[7] Buyukdagli S and Ala-Nissila T 2014 *J. Chem. Phys.* **140** 064701
[8] Netz R R and Orland H 2000 *Eur. Phys. J. E* **1** 203–14
[9] Lau A W C 2008 *Phys. Rev. E* **77** 011502
[10] Buyukdagli S and Ala-Nissila T 2014 *Langmuir* **30** 12907
[11] Buyukdagli S, Blossey R and Ala-Nissila T 2015 *Phys. Rev. Lett.* **114** 088303
[12] Coalson R D, Walsh A M, Duncan A and Tal N B 1996 *J. Phys. Chem.* **100** 2612
[13] Abrashkin A, Andelman D and Orland H 2007 *Phys. Rev. Lett.* **99** 077801
[14] Buyukdagli S and Ala-Nissila T 2013 *Phys. Rev. E* **87** 063201
[15] Buyukdagli S and Blossey R 2014 *J. Chem. Phys.* **140** 234903
[16] Xu Z and Maggs A C 2014 *J. Comput. Phys.* **275** 310–22
[17] Pujos J 2014 *PhD Thesis* ESPCI (unpublished)
[18] Deng M and Karniadakis G E 2014 *J. Chem. Phys.* **141** 094703
[19] Lee D J 2009 *Eur. Phys. J. E* **28** 419–40
[20] Wang R and Wang Z G 2013 *J. Chem. Phys.* **139** 14702
[21] Wang R and Wang Z G 2015 *J. Chem. Phys.* **141** 104705
[22] Buyukdagli S, Manghi M and Palmeri J 2010 *Phys. Rev. E* **81** 041601
[23] Buyukdagli S, Manghi M and Palmeri J 2011 *J. Chem. Phys.* **134** 074706
[24] Buyukdagli S, Achim C V and Ala-Nissila T 2011 *J. Stat. Mech.* P05033
[25] Buyukdagli S and Ala-Nissila T 2013 *J. Chem. Phys.* **139** 044907
[26] Clarke J, Wu H C, Jayasinghe L, Patel A, Reid S and Bayley H 2009 *Nat. Nanotech.* **4** 265–70
[27] Van der Heyden F H J, Stein D, Besteman K, Lemay S G and Dekker C 2006 *Phys. Rev. Lett.* **96** 224502
[28] Onsager L and Samaras N 1934 *J. Chem. Phys.* **2** 528
[29] Miles G, Cheley S, Braha O and Bayley H 2001 *Biochemistry* **40** 8514–22
[30] Gu L Q and Bayley H 2000 *Biophys. J.* **79** 1967–75
[31] Azuara C, Lindahl E, Koehl P, Orland H and Delarue M 2006 *Nucl. Acids Res.* **34** W38–42
[32] Azuara C, Orland H, Bon M, Koehl P and Delarue M 2008 *Biophys. J.* **95** 5597–605
[33] Koehl P, Orland H and Delarue M 2009 *Phys. Rev. Lett.* **102** 087801
[34] Koehl P and Delarue M 2010 *J. Chem. Phys.* **132** 064101
[35] Poitevin F, Orland H, Doniach S, Koehl P and Delarue M 2011 *Nucl. Acids Res.* **39** W184–9
[36] Levy A, Andelman D and Orland H 2012 *Phys. Rev. Lett.* **108** 227801
[37] Levy A, Andelman D and Orland H 2012 *J. Chem. Phys.* **139** 164909

[38] Smaoui M R, Poitevin F, Delarue M, Koehl P, Orland H and Waldispühl J 2013 *Biophys. J.* **104** 683–93

[39] Koehl P, Poitevin F, Orland H and Delarue M 2014 *J. Theory Comput. Chem.* **13** 1440001

[40] Buyukdagli S and Ala-Nissila T 2012 *Europhys. Lett.* **98** 60003

[41] Bonthuis D J, Gekle S and Netz R R 2011 *Phys. Rev. Lett.* **107** 166102

[42] Kornyshev A A and Sutmann G 1997 *Phys. Rev. Lett.* **79** 3435

[43] Hildebrandt A, Blossey R, Rjasanow S, Kohlbacher O and Lenhof H P 2004 *Phys. Rev. Lett.* **93** 108104

[44] Maggs A C and Everaers R 2006 *Phys. Rev. Lett.* **96** 230603

[45] Bonthuis D J and Netz R R 2012 *Langmuir* **28** 16049

[46] Bonthuis D J and Netz R R 2013 *J. Phys. Chem.* B **117** 11397

[47] Ballenegger V and Hansen J P 2005 *J. Chem. Phys.* **122** 114711

[48] Blum L and Henderson D 1981 *J. Chem. Phys.* **74** 1902

[49] Buyukdagli S and Blossey R 2014 *J. Phys.: Condens. Matter* **26** 285101

[50] Buyukdagli S 2015 *J. Phys.: Condens. Matter* **27** 455101